

A Practical Guide to using Pauli Path Simulators for Utility-Scale Quantum Experiments

Hrant Gharibyan¹, Siddharth Hariprakash^{1,2,3}, Mohammed Zuhair Mullath¹, and Vincent P. Su¹

¹BlueQubit Inc, San Francisco, CA 94105, USA

²Leinweber Institute for Theoretical Physics and Department of Physics, University of California, Berkeley, California 94720, USA

³Physics Division, Lawrence Berkeley National Laboratory, Berkeley, California 94720, USA

July 16, 2025

Abstract

In this paper we present an inexpensive protocol to perform runtime and memory estimation for large-scale experiments with Pauli Path simulators (PPS). Additionally, we propose a conceptually simple solution for studying whether PPS can be used as a scientific discovery tool, rather than reproducing existing answers.

We start by analyzing the dynamics of the Pauli coefficients tracked in the Heisenberg picture. In addition to surprisingly generic convergence features of the coefficient distributions, we find certain regularities that allow for extrapolation of memory and runtime requirements for smaller and smaller coefficient truncation parameter δ .

We then introduce a framework for understanding convergence in the absence of rigorous error guarantees on PPS. Combined with runtime analysis, we propose bifurcating quantum simulation problems broadly into two classes, based on whether there is apparent convergence of expectation values as a function of δ . This serves as a way for practitioners to understand where their problem falls on the frontier of classical simulability. In the case without apparent convergence, PPS may still serve useful as a Monte Carlo-like estimate. Applied to IBM's utility-scale experiments, we show parameter regimes where both behaviors are realized. Some of our key findings challenge conventional intuition: reducing δ does not always improve accuracy, and deeper quantum circuits may actually be easier to simulate than shallower ones.

Our analysis provides the first systematic approach to assess PPS reliability *without* assuming a groundtruth quantum answer. The BlueQubit SDK implementing these methods has been released publicly, offering researchers a comprehensive toolkit for evaluating this frontier classical simulation approach. These results establish practical guidelines for when PPS can serve as a reliable verification tool versus when it should be used as a complementary estimate alongside quantum experiments.

Contents

1	Introduction	2
2	The Branching and Merging Dynamics of PPS	3
3	Modeling the Proliferation of Pauli Operators	5
3.1	Evolution of the distribution of Pauli coefficients	5
3.2	Bounding the growth of Pauli terms	6
3.3	A resource efficient method to estimate N_{\max}	9
4	Scrutinizing convergence of PPS	10
4.1	Apparent Convergence of PPS	11
4.2	Beyond Apparent Convergence	12

5 Discussion	14
A PPS Convergence with BlueQubit Backend	17
B Bit efficient representation of Pauli sums	18
C Coefficient distribution for correlated angles	18
D Analytical results on Pauli Proliferation	18
E Deviations from a Power Law caused by η-spikes	23
E.1 Transient deviations	23
E.2 Small angles and persistent deviations	25
F Challenges in estimating the power-law exponent m	25

1 Introduction

Simulating quantum systems remains one of the central challenges in computational physics, computational chemistry, and quantum information science. Despite the exponential growth of Hilbert space with system size, classical simulation methods continue to provide essential insights into quantum dynamics, verification of quantum hardware, and development of novel quantum algorithms. While tensor network methods [Vid03, HCO⁺11, Orú14, HLO⁺16, BB17] and their variants [TFSS24, TF23] have long dominated this space – particularly for low-entanglement systems – recent innovations have begun to chart alternative directions that can tackle problems outside the reach of conventional approaches.

One such innovation is the Pauli Path Simulation (PPS) framework,¹ which has emerged as a powerful method for simulating quantum systems in the Heisenberg picture. Instead of evolving quantum states forward in time – as done in traditional statevector based simulations – PPS propagates observables backward through a quantum circuit. The observable is decomposed into a sum of Pauli strings, and its evolution is approximated by sampling and propagating the most significant terms along discrete Pauli paths determined by the circuit unitaries. While a full expansion involves up to 4^n Pauli terms for an n -qubit system – compared to 2^n amplitudes in the Schrödinger picture – this exponential overhead can be mitigated through judicious truncation strategies that preserve accuracy while greatly reducing computational cost.

Originally inspired by the NISQ era quantum computers – where quantum circuits are often shallow and dominated by noise – it is natural to consider the *size*, or Hamming weight, of Pauli operators when deciding which terms to truncate. One of the simplest truncation schemes is to discard operators that act non-trivially on more than k qubits. For instance, [SWCL24, FRD⁺25, SYGY24, AGL⁺23, AMR⁺25] show that the error introduced by this approximation decays exponentially with increasing k . This result was later extended to an ensemble of noiseless circuits as well (see, e.g., [ASR⁺24, LPR⁺24]). Since its initial conception, additional approximation strategies have been explored, such as *coefficient-based truncation* [BGC23, BcvacC25], where Pauli terms with amplitudes below a specified threshold, δ , are systematically discarded. More recently, Rudolph et al. [RJT⁺25] presented a comprehensive account of Pauli propagation methods, including their mathematical foundations, truncation strategies, and practical implementation as a Julia package.

One of the first notable experimental applications of Pauli Path simulations was performed in [BC23] to reproduce the expectation values in a 127 qubit dynamical quantum kicked Ising model, originally obtained using IBM hardware [K⁺23]. While statevector simulation is limited to a few dozens of qubits, even other leading approximations such as generic tensor network-based matrix product states failed to correctly capture the entanglement at later stages of the time evolution, hinting at a potential demonstration of classical intractability.² However, as is typical, new quantum results lead to innovation on the classical algorithm side as well, prompting others to reproduce the results with very moderate resources.

PPS introduces a critical question that has received limited systematic attention: When can we trust the results? Unlike exact simulation methods, PPS relies on approximations whose errors are difficult to bound a priori. A smaller truncation threshold δ should in principle yield more accurate results, yet

¹Also commonly referred to as Pauli propagation or Sparse Pauli Dynamics (SPD) framework.

²Only highly specialized tensor network approaches [TFSS24] tailored to IBM’s specific heavy-hexagon connectivity yielded approximate agreement.

our investigations reveal this intuition to be misleading. Similarly, one might expect deeper quantum circuits to be universally harder to simulate, but we find examples where the opposite holds true. These counterintuitive behaviors point to a fundamental gap in our understanding of when and how PPS can reliably estimate quantum observables.

Our primary goal of this paper is to provide a practical framework that helps quantum researchers evaluate the utility of PPS for their problem. In addition to serving as a pedagogical text for an overview of this method, we present crucial memory and runtime analysis that will help users better understand the computational resources required to deploy this method. An often overlooked aspect of PPS is the fluctuation of expectation values as a function of the truncation parameter. Combined with a lack of practical error bounds, this can make PPS less reliable as a discovery tool, but still valuable as a complement to quantum hardware runs. Our framework involves studying this convergence with extremely modest CPU resources to diagnose whether PPS has *apparently* converged and also to extrapolate the computational demands of finer-resolution simulations. We also introduce the newly integrated BlueQubit SDK for Python, which enables scalable PPS simulations with minimal infrastructure requirements. As a practical demonstration, we include a working code snippet that applies our convergence framework to IBM’s utility circuit in App. A.

For researchers considering classical simulation approaches, a natural question arises: when should one choose PPS over tensor network methods? Currently, neither approach strictly dominates the other across all simulation scenarios. The methods exhibit complementary strengths depending on the specific computational task. When evaluating multiple observables for a given circuit, PPS requires separate runs for each observable, while tensor network methods typically compute a single approximate time-evolved state from which multiple expectation values can be efficiently extracted. However, this advantage comes with trade-offs in complexity: for the most challenging simulation problems, tensor networks often require extensive tuning of bond dimensions, contraction schemes, and network architectures, whereas Pauli propagation offers more straightforward control through relatively simple truncation parameters.

Paper Organization: The remainder of this paper is structured as follows. Section 2 presents an accessible overview of the PPS technique, emphasizing the branching mechanism that drives computational complexity. Section 3 develops our theoretical framework for predicting resource requirements, revealing the general power-law structure of coefficient distributions and demonstrating how this enables accurate extrapolation of memory and runtime costs from brief, inexpensive experiments. Section 4 introduces our convergence assessment protocol and applies it systematically to IBM’s kicked Ising circuits, revealing the two distinct regimes where PPS either apparently converges or provides useful Monte Carlo-like estimates. Throughout, we emphasize the counterintuitive findings that challenge conventional assumptions about classical simulation. Section 5 discusses the broader implications for quantum computing and the role of PPS in distinguishing between classically tractable and genuinely quantum-advantaged problems.

2 The Branching and Merging Dynamics of PPS

In this section, we provide an overview of the PPS simulation technique used to generate the numerical results presented in this work.³ At the highest level, this is simply working backwards through a circuit, applying the Heisenberg picture to an observable one gate at a time. This step-by-step procedure can be thought of as a flow from Pauli terms with large coefficients to many more Pauli terms with smaller coefficients. This intuitive picture will be made more concrete numerically in Section 3.

In the standard Schrödinger picture of quantum mechanics, states evolve while observables remain fixed. For a quantum circuit applied to an initial state $|\psi_0\rangle$. In this work, we set $|\psi_0\rangle = |0\rangle$ and hence computing the expectation value of an observable O requires:

$$\langle O \rangle = \langle 0 | U^\dagger O U | 0 \rangle, \quad (1)$$

where U represents the unitary transformation of the entire circuit. Most common quantum simulation approaches track evolution of the quantum state storing an exponentially large statevector. The PPS method instead employs the Heisenberg picture, where observables evolve backward through the circuit while states remain fixed:

$$\langle O \rangle = \langle 0 | U^\dagger O U | 0 \rangle = \langle 0 | O(t) | 0 \rangle, \quad (2)$$

where $O(t) = U^\dagger O U$ represents the time-evolved observable. This transformation allows us to calculate expectation values without explicitly storing the full quantum state.

³For additional description of the technique, see for example [BGC23, BcvacC25, RJT⁺25].

Without loss of generality, the n -qubit unitary U representing the unitary transformation of a given circuit can be represented as a series of Pauli rotations as follows:

$$U = \prod_{j \in [J]} U_j(\theta_j) = \prod_{j \in [J]} e^{-i\theta_j \sigma_j / 2}, \quad (3)$$

where each σ_j is an n -qubit Pauli operator, and each $\theta_j \in [-\pi/4, \pi/4]$. The restriction on the angles θ_j can be accomplished using the method of Clifford recompilation as described for example in [QWE19, BC23].

Let O_k be the observable after the action of k gates:

$$O_k := U_k^\dagger U_{k-1}^\dagger \dots U_1 O U_1 U_2 \dots U_k. \quad (4)$$

Using the Pauli basis, O_k can always be decomposed as

$$O_k = \sum_{P \in \mathcal{P}_k} c_P^{(k)} P, \quad (5)$$

where \mathcal{P}_k is a subset of all possible n -qubit Pauli operators with non-zero coefficients.

The key to understanding PPS behavior lies in how Pauli operators interact with circuit gates. We partition the Pauli terms based on their commutativity with the next gate generator σ_{k+1} :

$$\mathcal{P}_k^{comm} := \{P \in \mathcal{P}_k \mid [P, \sigma_{k+1}] = 0\}, \quad (6)$$

$$\mathcal{P}_k^{anti} := \{P \in \mathcal{P}_k \mid \{P, \sigma_{k+1}\} = 0\}. \quad (7)$$

This partition determines the computational cost: commuting terms pass through unchanged, while anti-commuting terms branch, possibly creating new Pauli strings. Specifically:

$$U_{k+1}^\dagger P U_{k+1} = \begin{cases} P & \text{if } P \in \mathcal{P}_k^{comm} \\ \cos(\theta_{k+1})P + \sin(\theta_{k+1})P' & \text{if } P \in \mathcal{P}_k^{anti}. \end{cases} \quad (8)$$

Here, $P' = i\sigma_{k+1}P$ is the conjugated Pauli string. This branching is the fundamental source of exponential growth in PPS simulations—each anti-commuting term potentially doubles the number of tracked operators. Thus, the size of the relevant set of Paulis grows as $\mathcal{P}_{k+1} = \mathcal{P}_k \cup \sigma_{k+1}\mathcal{P}_k^{anti}$.

The coefficient evolution follows a branching-and-merging pattern. For a Pauli term P , its updated coefficient $c_P^{(k+1)}$ depends on multiple factors: whether it existed before the gate, whether it commutes with the gate, and whether other terms branch into it: Using that $\sigma_{k+1}^2 = 1$, this merging can be pre-determined by checking whether $P' = i\sigma_{k+1}P \in \mathcal{P}_k^{anti}$.

More explicitly,

$$c_P^{(k+1)} = \begin{cases} c_P^{(k)} & \text{if } P \in \mathcal{P}_k^{comm} \\ c_P^{(k)} \cos(\theta_{k+1}) & \text{if } P \in \mathcal{P}_k^{anti} \text{ and } P' \notin \mathcal{P}_k \\ c_P^{(k)} \cos(\theta_{k+1}) + c_{P'}^{(k)} \sin(\theta_{k+1}) & \text{if } P \in \mathcal{P}_k^{anti} \text{ and } P' \in \mathcal{P}_k \\ c_{P'}^{(k)} \sin(\theta_{k+1}) & \text{if } P \notin \mathcal{P}_k \text{ and } P' \in \mathcal{P}_k^{anti} \end{cases} \quad (9)$$

In this manner, the Pauli decomposition of the evolved observable can be iteratively updated by traversing through (in order) and evolving the observable by the unitaries U_j . Generically, this will lead to a proliferation of terms stemming from the anti-commuting set. However, in the case of Clifford operations, the angles will be restricted to special values that prevent this branching. Hence, the presence of a large number of non-Clifford operations can lead to rapid growth in the total number of terms present in the Pauli decomposition of the evolved observable. For details on representing the Pauli strings with bit arrays, see Appendix B.

Up to this point, the simulation technique is exact as every possible term arising throughout the evolution has been accounted for. The approximation made by the PPS method is to impose a $\delta \in \mathbb{R}^+$ truncation on the norms of the coefficients in the Pauli basis of the evolved observable at any given step in the evolution. Thus, the coefficients $c_P^{(k)}$ appearing in Eq. (5) are now required to satisfy $|c_P^{(k)}| \geq \delta$. Upon evolving the observable O_k by the unitary U_{k+1} , we truncate the Pauli decomposition shown in Eq. (8) by imposing the condition $|c_P^{(k+1)}| \geq \delta$. In this manner, one can control the (in general) exponential growth in the number of terms appearing in the Pauli decomposition of the evolved observable.

Though straightforward from Eq. (9), we note the fact that the coefficients are always decreasing in magnitude based on these dynamics. Because it will be useful in the following section, consider treating

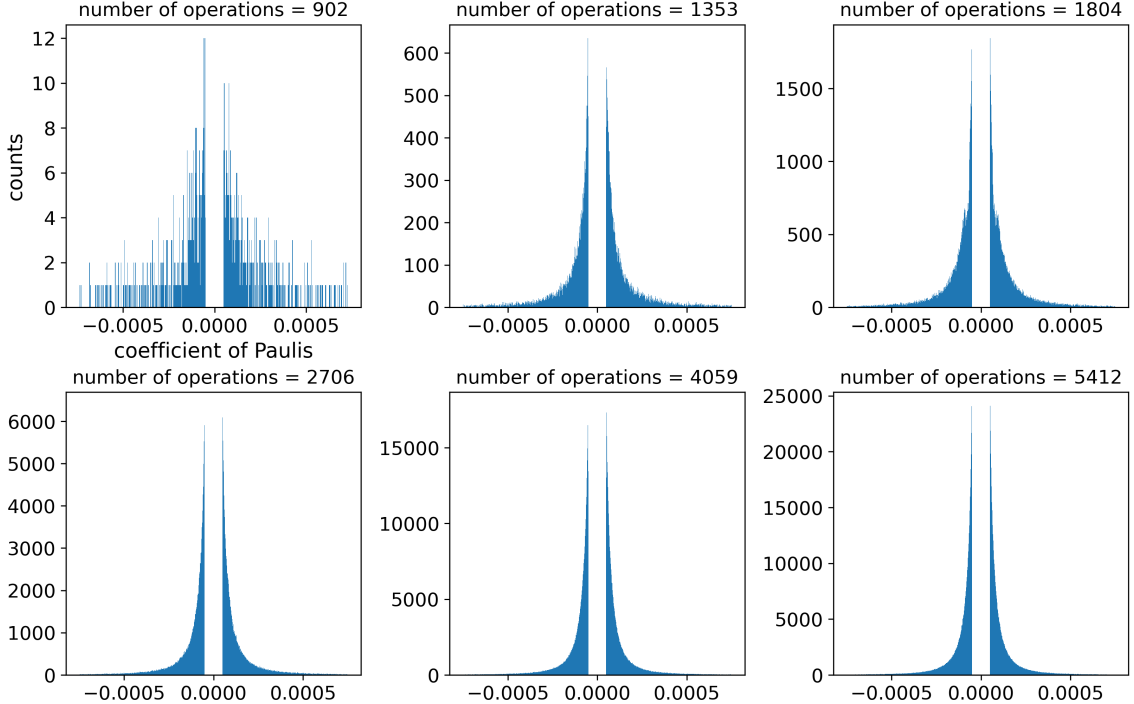


Figure 1: Evolution of the distribution of Pauli coefficients shown at different stages in the execution of a circuit of the form Eq. (10) with each θ_X chosen by sampling uniformly from $[-\pi/4, \pi/4]$, $\theta_{ZZ} = -\pi/2$, $T = 20$, and a coefficient threshold $\delta = 5 \times 10^{-5}$. We set the initial observable to be the single weight operator $\langle Z_{62} \rangle$ and observe that upon evolving using sufficiently many gate operations, the distribution appears to possess some invariant structure.

the sum Eq. (5) as a continuous density over coefficients. A single gate application only has a discrete set of possibilities for affecting a given coefficient, and hence for its impact on the density. In the limit where every angle in the circuit is the same, the density will be a series of Dirac δ spikes. In the opposite limit, if the angles are generically uncorrelated, then we find that this density can actually be well-modeled by a power law. It turns out the latter is a more generic behavior.

3 Modeling the Proliferation of Pauli Operators

This section presents our framework for understanding and predicting the computational resource requirements of Pauli Path Simulators with coefficient truncation. The core challenge we address is determining whether a quantum circuit can be simulated within available memory and time constraints before committing to expensive computational runs. Our analysis reveals that the seemingly complex dynamics of Pauli string proliferation can be modeled by surprisingly simple mathematical patterns.

In particular, we show a simple observation regarding the distribution obeyed by the coefficients of the evolved observable in the Pauli basis enables accurate predictions of memory and runtime requirements for a class of circuits. For the researcher interested in applying PPS to their quantum circuit calculation, we translate these theoretical insights into a practical algorithm for predicting resource needs using only brief test runs.

A word on notation: For an observable O with Pauli-sum representation $\sum_P c_P P$ in the *unnormalized* n -qubit Pauli basis, we shall be writing $\|O\|$ to denote the “raw norm” of O given by $(\sum_P |c_P|^2)^{1/2}$. It is related to the standard Hilbert-Schmidt norm by $\|O\|_2 = (\text{Tr}(O^\dagger O))^{1/2} = 2^n \|O\|$.

3.1 Evolution of the distribution of Pauli coefficients

We start by considering the kicked Ising dynamics studied by IBM in [K⁺23] on quantum hardware as well as in [TFSS24, LWZ⁺23, PJSO24] using state of the art tensor network methods. This Hamiltonian

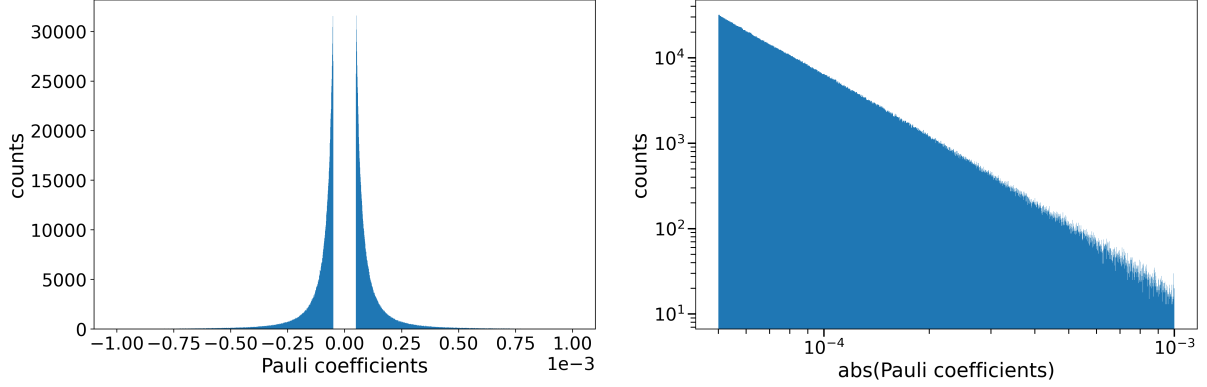


Figure 2: (left) Distribution of Pauli Coefficients corresponding to the set up described in Fig. 1 and (right) the distribution of the absolute values of these coefficients. The data shown was captured after the execution of 5412 out of the 5420 total gates in the circuit. There are approximately 2.5 million unique Paulis present in the evolved observable and we use 2048 bins to plot the histograms. The distribution shown on the right can be approximated by a power law with larger deviations towards the tail.

simulation problem amounts to implementing unitaries of the form

$$U = \prod_{t \in [T]} \left(\prod_{\langle i, j \rangle} e^{-i\theta_{ZZ} Z_i Z_j / 2} \prod_i e^{-i\theta_X X_i / 2} \right), \quad (10)$$

where T denotes the total number of Trotter steps in the evolution and $\langle i, j \rangle$ indicates nearest neighbors on IBM's 127 qubit heavy hex lattice. In existing literature, θ_X is generally fixed to be a constant throughout a single circuit instance (i.e. the single qubit rotation gates are chosen to be correlated). However, to break translation invariance and give a slightly more generic circuit, in this section we consider the case where we choose each of the single qubit rotation angles θ_X by sampling uniformly from $[-\pi/4, \pi/4]$ ⁴. This randomly generated case more closely resembles a broader class of brickwork variational circuits. As in previous work, we set $\theta_{ZZ} = -\pi/2$, i.e. the two-qubit rotations are chosen to be correlated and Clifford.

Throughout this work, we will set the initial observable $O = Z_{62}$. For a depth $T = 20$ circuit we evolve O using the unitary shown in Eq. (10) and plot the distribution of Pauli coefficients of the evolved observable at different stages in the circuit evolution in Fig. 1. From Eq. (9) we expect that the circuit operations will make the Pauli coefficients of the evolved observable smaller (in magnitude), thus explaining the increasing concentration at smaller (in absolute value) coefficient values as we traverse the circuit. About a third of the way through the circuit, we observe that the shape of this distribution looks roughly invariant. Focusing on a point in the evolution after which the shape of this distribution of Pauli coefficients appears invariant, we see that the absolute values of these Pauli coefficients (see Fig. 2) appear to be well approximated by a truncated power law of the form

$$\rho(t) = \frac{A}{|t|^{m+1}}, \quad |t| > \delta, \quad (11)$$

where A is a normalization constant, given by $A = m\delta^m/2$. In Appendix D we demonstrate similar behavior if we instead set $\theta_X = \pi/4$ i.e. maximally non Clifford and show that upon making mild assumptions about the similarity of the sets $\mathcal{P}_k^{\text{comm}}$ and $\mathcal{P}_k^{\text{anti}}$ one can show that such a power law density yields a steady state solution to the dynamics specified by Eq. (9).

3.2 Bounding the growth of Pauli terms

In this section, we use the specific form of the power law shown in Eq. (11) to understand the growth of the number of unique Paulis present in the evolved observable as a function of the number of gate operations used to perform the evolution. In particular, Fig. 3 shows examples of such *Pauli growth*

⁴Appendices C and D provide numerical evidence suggesting that our findings in this section can be extended to the correlated case as well with some caveats as explained in Appendix E.2

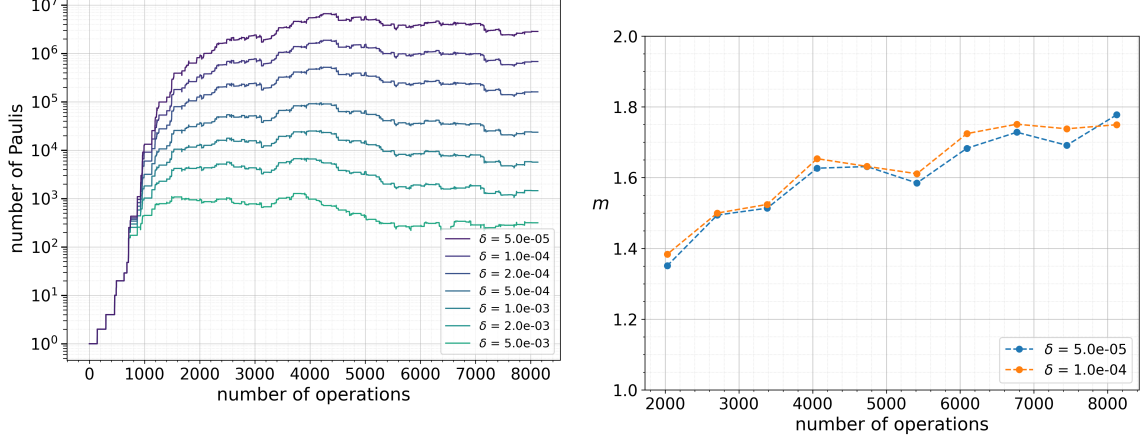


Figure 3: Tracking the growth of Pauli's and the shape of the power-law coefficient distribution. Left: growth of number of Pauli terms in the simulation with θ_X sampled uniformly from $[\pi/4, \pi/4]$, $\delta = 5 \times 10^{-5}$, $T = 30$; right: power-law exponent m varies over the execution of the same circuit. The values of m are estimated directly from the coefficient distribution of Pauli terms at various points in the circuit execution. For more details about this fit, see Appendix F.

curves along with the variation in the power law parameter m as a function of the number of gate operations. There are two interesting observations we make from this set of plots.

1. The shapes of the Pauli growth curves (after sufficiently many gate applications) appear roughly similar with vertical shifts that look regular with variations in δ . We also note that the maximum of each curve throughout the evolution, denoted by N_{\max} , also visually appears to be regularly spaced on the vertical axis as a function of δ . Fig. 11 shows more examples of this observations using different experimental setups.
2. The parameter m that determines the exact form of the power law Eq. (11), as shown on the right, exhibits variations as a function of both δ and the number of gate applications.

In this section, we provide one possible explanation for the first observation. In Appendix D we identify key parameters that explain why the growth curves, although similar, show minor deviations from each other. For more on the second observation as well as subtleties that arise when estimating m see Appendix F.

We begin by observing that imposing the constraint that all surviving terms post truncation have magnitude greater than δ , the following trivial bound holds:

$$N_{\max} \leq \frac{\|O\|^2}{\delta^2} \quad (12)$$

To improve on this analysis, we observe that the average value of the sum computing the norm $\|O_k\|^2$ (where O_k is the evolved observable given by Eqs. (4) and (5)) is a Riemann sum approximation of the second moment of the distribution of the absolute values of the Pauli coefficients ρ :

$$2 \int_{\delta}^{\|O\|} t^2 \rho(t) dt \approx \frac{1}{N_k} \sum_{P \in \mathcal{P}_k} |c_P^{(k)}|^2 = \frac{\|O_k\|^2}{N_k}. \quad (13)$$

Using the general definition of ρ , given by Eq. (11), we thus have that (note the k dependence on m has been assumed due to the second observation made based on Fig. 3):

$$m_k \delta^{m_k} \int_{\delta}^{\|O\|} t^2 \frac{dt}{t^{m_k+1}} \approx \frac{\|O_k\|^2}{N_k} \quad (14)$$

$$\Rightarrow N_k \approx \frac{2 - m_k}{m_k} \frac{\|O_k\|^2}{\delta^{m_k} (\|O\|^{2-m_k} - \delta^{2-m_k})}, \quad (15)$$

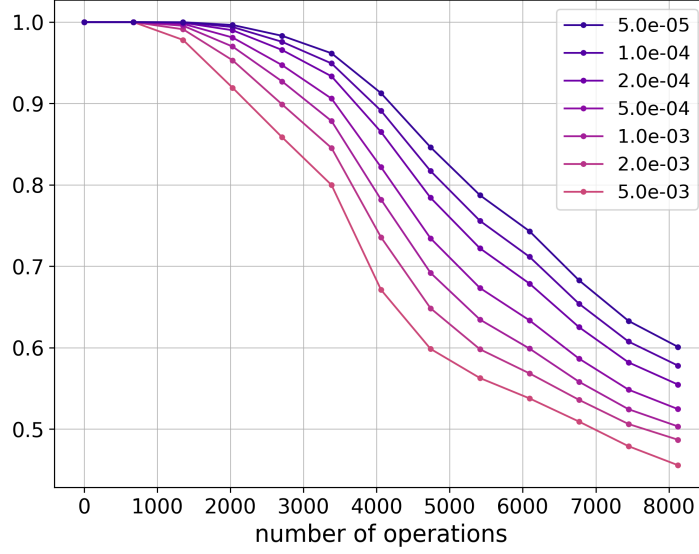


Figure 4: Decrease in the norm $\|O_k\|$ of the evolved observable over the execution of the circuit for various values of truncation threshold. The circuit was constructed with θ_X sampled uniformly from $[\pi/4, \pi/4]$ and $T = 30$.

Let m^* be the maximum m over the course of the circuit and k^* be the k -th gate where m^* is achieved

$$m^* := \max_{k \in [J]} m_k, k^* := \operatorname{argmax}_{k \in [J]}(m_k), \quad (16)$$

If for simplicity we assume $\|O\| = 1$ and that variations in the error made by the Riemann sum approximation as a function of δ and k are sub-leading to the other effects we consider, we then have the following result for the maximum number of unique Pauli terms at any given point in the evolution (assuming that δ is chosen such that the evolution is in the regime where N_{\max} has not reached the worst case scaling of 4^n for an n -qubit system):

$$N_{\max} \approx \frac{2 - m^*}{m^*} \frac{\|O_{k^*}\|^2}{\delta^{m^*}(1 - \delta^{2-m^*})}, \quad (17)$$

An important consequence of Eq. (17) is that gaps between Pauli-growth curves such as those shown in Fig. 3 can be shown to be approximately regular with respect to variations in δ . In particular, we have that

$$\log \left(\frac{N_{\max}(\delta_1)}{N_{\max}(\delta_2)} \right) \approx m^* \log \left(\frac{\delta_2}{\delta_1} \right) + 2 \log \left(\frac{\|O_{k^*}(\delta_1)\|}{\|O_{k^*}(\delta_2)\|} \right) + \log \left(\frac{1 - \delta_2^{2-m^*}}{1 - \delta_1^{2-m^*}} \right). \quad (18)$$

When δ_1 and δ_2 are small, Eq. (18) can be further approximated as follows:

$$\log \left(\frac{N_{\max}(\delta_1)}{N_{\max}(\delta_2)} \right) \approx m^* \log \left(\frac{\delta_2}{\delta_1} \right) + 2 \log \left(\frac{\|O_{k^*}(\delta_1)\|}{\|O_{k^*}(\delta_2)\|} \right) \quad (19)$$

As shown in Fig. 4, when variations in δ are small so are the variations in the norm $\|O_k\|$ and hence we expect the behavior of the LHS of Eq. (19) to be mostly characterized by the first term on the RHS. In other words, uniform (multiplicative) changes in δ approximately lead to uniform (multiplicative) changes in N_{\max} .

We end this section by noting that since $\|O_k\| \leq \|O\| = 1$, Eq. (17) can be written as:

$$N_{\max} \lesssim \frac{2 - m^*}{m^*} \frac{1}{\delta^{m^*}(1 - \delta^{2-m^*})}, \quad (20)$$

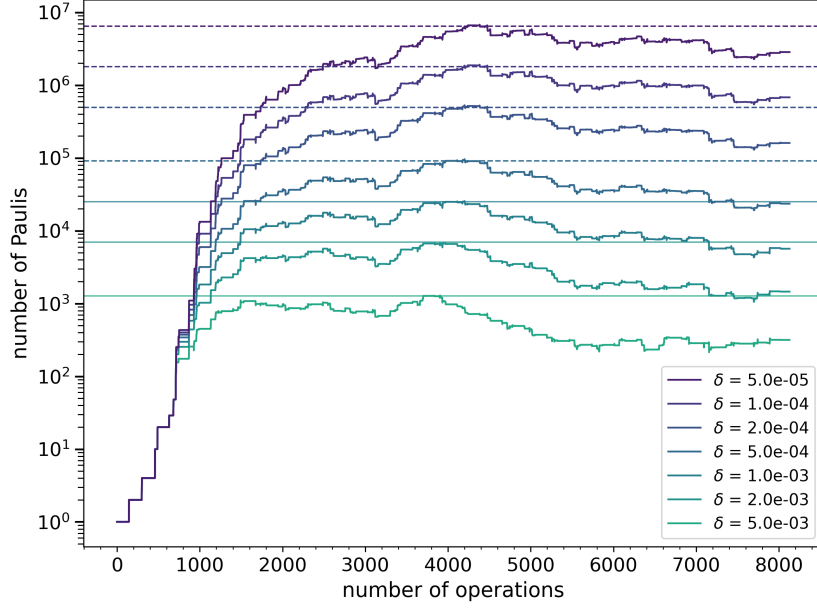


Figure 5: Estimating N_{\max} via extrapolation : The exact values of N_{\max} corresponding to the three largest values of δ (solid horizontal lines) are used to extrapolate and predict N_{\max} for the smaller values of δ indicated in the plot. The predictions are within 6% of the true N_{\max} values. The circuit used is constructed with each θ_X sampled uniformly from $[-\pi/4, \pi/4]$ and $T = 30$.

where we use \lesssim to denote an upper bound up to a constant factor. We also note that using the bound shown in Eq. (15), we can estimate other (absolute) moments of the coefficient distribution. For any $l \geq 1$, we get:

$$\sum_{P \in \mathcal{P}_k} |c_P^{(k)}|^l \approx \frac{(2 - m_k)}{(l - m_k)} \frac{(1 - \delta^{(l - m_k)})}{(1 - \delta^{(2 - m_k)})} \|O_k\|^2. \quad (21)$$

These estimates also show the dependence of the resources required to compute the evolved observable O_k on the power-law exponent m . For example, the fourth-moment is called *generalized Pauli purity* and is related to magic resources; see Theory Box 6 in [RJT⁺25] and the references therein for more details.

3.3 A resource efficient method to estimate N_{\max}

In this section, we present numerical results demonstrating that Eqs. (18) and (19) serve as a useful tools for predicting memory requirements at finer resolution. Directly using Eq. (17) for instance can prove to be challenging since this requires accurate estimates of the power law exponent m , which as we show in Appendix F can prove to be a non-trivial problem. Furthermore, any relative error in m leads to a relative error in N_{\max} multiplied by $|\log(\delta)|$.⁵

Importantly, while our theoretical analysis provides insight into this observed regularity, we show that the logarithmic consistency enables a powerful numerical bootstrapping approach: we can extrapolate simulation requirements from coarser truncation thresholds (larger δ) to predict resource needs at finer thresholds (smaller δ), dramatically reducing the computational cost of resource estimation. In practical terms, a scientific user would run this Pauli curve for very coarse thresholds at a cheap price and successively decrease δ by some constant ratio r . If the curves look similar then one can use this ratio r to extrapolate N_{\max} with a simple linear regression. Empirically, we find that getting just a few data points with $\delta_0 \approx 0.005$, $r = 1/\sqrt{2}$ is a good starting point. For Fig. 5, we obtained $\hat{N}_{\max}(\delta)$ in less than a minute on a 6-core CPU with less than 6% error on the N_{\max} obtained by running the full Pauli Path simulation.

As another check of the predictive power of this method, we also apply this resource estimate to the 2D Ising dynamics on an 11×11 square lattice with open boundary conditions studied in Ref. [BcvacC25]. In particular, we implement the first order Trotterization (Eq. 19 of [BcvacC25]) with $h = 3.044382$, $t = 0.92$, and $\Delta t = 0.04$ and perform PPS runs with 5 values of δ starting from $\delta_0 = 2^{-12}$ with

⁵For a 5% error in estimating m and a $\delta = 5 \times 10^{-5}$ this could potentially mean a 50% error in the N_{\max} prediction.

$r = 1/\sqrt{2}$. Our generated estimate for N_{\max} is ~ 2.1 billion and 48.5 hours for the runtime⁶. The reported value N_{\max} in Fig. 8 of Ref. [BcvacC25] appears to be roughly 2.5 billion. We note that the estimation procedure takes just under 7 min on a single CPU core, providing valuable runtime and memory information. This yields a ballpark estimate even though this particular example results in the distribution of the absolute values of the coefficients exhibiting larger deviations from a power law form than that shown in for instance in Fig. 2. For a discussion of these deviations, see Appendix E.2.

We end this section by pointing out some potential sources of errors that can skew such N_{\max} estimates. The first is that the tail of the distribution contributes significantly to the second moment estimate in Eq. (13) (as in the inset of Fig. 16 where we provide an explicit numerical example of this effect). If the tail then also exhibits large deviations from a power law this might skew N_{\max} estimates. Second, if N_{\max} occurs close to the end of the circuit in the test runs, then the estimates can be less accurate in some cases as we only have a partial picture of the Pauli growth curves. (We speculate this is related to the small but visually apparent horizontal “drift” of N_{\max} from one δ to the next as seen for example in Fig. 11).

4 Scrutinizing convergence of PPS

Notably, PPS suffers from a lack of useful error bounds as δ decreases. The question of convergence as a function of the truncation parameter δ has been mentioned in other works (most notably in [BC23]), but mostly with a focus on finding the largest (cheapest) δ approximation which achieves a certain desired result.

We flip the investigation around and seek to understand when this classical method appears reliable and where it points to its own shortcomings. Even when PPS fails to converge, it can still be useful as an independent estimate to hardware runs, especially in the age of quantum devices that require sophisticated error mitigation techniques that need tuning to extract answers with confidence.

As in the last section, the main protocol we propose is tracking the convergence of a given expectation value for finer truncation parameter, starting with a rather coarse δ . This gives a way to start with modest computational resources before choosing to commit to a large simulation which may or may not yield a reliable answer. We find that the simulation time scales as a power law in $1/\delta$, leading to an efficient way to estimate the CPU time needed to extend to smaller δ .

For notational convenience, we define a few variables. δ_0 an initial, relatively large truncation parameter, r is the ratio between successive δ_n , t_{CPU} is the maximum wall time. Let \mathcal{O}_n denote the observable expectation value with truncation parameter δ_n and t_n denote the simulation time for computing \mathcal{O}_n . Let ε_{tol} denote a convergence tolerance.

The protocol can then be summarized succinctly as follows. Compute successive estimates \mathcal{O}_n using $\delta_n = r^n \delta_0$ and proceed until t_n exceeds t_{CPU} or ℓ successive estimates of \mathcal{O}_n converge to within ε_{tol} . Because of the power law scaling of time vs δ , one can also predict how long experiments with larger δ_n will take.

Since PPS is a frontier classical simulation method, it necessarily makes some problems look easy while struggling with other. One goal of this paper is to bifurcate quantum simulation problems by looking at convergence patterns. In the first category are problems where taking successively small δ_n leads to apparent convergence. Here, we use the term apparent convergence since there are no guarantees that finer and finer resolutions will yield the same value, unless all terms are kept. There may be many small-scale fluctuations so that the technical definition of convergence may very sensitively depend on ε_{tol} . However, in those cases it may still lead to high confidence in the resulting answer.

The second category is composed of problems for which, under finite t_{CPU} , the approximate expectation value fluctuates wildly, and estimates can no longer be trusted to have a high level of accuracy. Surprisingly, some of the results reproducing expectation values the IBM experiment [K⁺23] belong to this class. Without the hardware result, PPS applied to those problems would not yield a reliable answer. However, if the PPS answer was calculated before the quantum result, it would still lead to a guiding range of where the true expectation should lie.

In both cases, the simulation time scales as a power law in $1/\delta$ (for sufficiently small δ). Thus, given finite computational resources, one can always check convergence based on coarser δ and use those runtimes and N_{\max} values to extrapolate the resource requirements for pushing to finer δ .

As a preview of this section, we highlight some surprising results on the utility of PPS.

⁶The extrapolation in runtime can be done using the simple power law scaling as a function of δ that we explore in Section 4

1. For some instances where PPS reproduced published IBM results, it looks far from converged.
2. Even when unconverged, PPS may still be useful in tandem with results from quantum hardware, for example, serving as a Monte Carlo-like estimate.
3. Exact simulation is obtained as $\delta \rightarrow 0$, but simulations with smaller δ do not always get closer to the exact answer.
4. Conversely, extending a given circuit to larger depth may actually lead to PPS converging with *fewer resources*.

4.1 Apparent Convergence of PPS

We now turn our attention to studying the convergence of expectation values with PPS. As a classical approximation method, there is inherently some level of precision sacrificed. However, it is important to note that even with a quantum device, the presence of errors, whether from gate fidelities, measurement readout or simply statistical shot noise, there are always error bars present in the final quantum result.

It may then be tempting to simply ask for convergence of PPS within error bars comparable to those present from quantum devices. Because convergence depends very sensitively on ε_{tol} and the ratio between successive δ_n , r , there is some trial and error needed. Additionally, this is further complicated since the error induced by the truncation is non-monotonic.

As an example, we apply our protocol to the kicked quantum dynamics with the single site observable $\langle Z_{62} \rangle$. For random single qubit rotations and varying number of Trotter steps, we see that extending PPS beyond $\delta = 10^{-3}$ does not significantly change the estimate. See Fig. 6.

There are a number of interesting observations about this convergence behavior. First, we see the sensitivity to ε_{tol} . For the same choice of $\delta_0, r, t_{\text{CPU}}$, decreasing ε_{tol} from 10^{-2} to 10^{-3} , one needs to decrease δ by almost 2 orders of magnitude. Correspondingly, the largest t_n at $T = 24$ was over 100 times larger without officially converging, even when using 64 CPU cores vs a single core⁷. Based on this clear power law scaling of the time, we can extrapolate that the next two points would take 20 hours and 50 hours, respectively.

Here, the extra computational resources simply confirm the confidence in the convergence, but do not change the result⁸. Decreasing δ in principle should approach the correct answer since $\delta \rightarrow 0$ corresponds to exact simulation. In practice, the lack of control on the signs of the corrections highlights a key feature about using PPS. Picking a smaller δ does not always yield a more useful result. If running for one day gives the same level of approximation as running it for 1 minute, then cheaper is better.

Another salient aspect of the convergence in Fig. 6 is that a deeper circuit does not necessarily imply that one needs a smaller δ to achieve comparable accuracy than the δ needed for the shorter circuit. Compare the case of $T = 12$ versus $T = 24$ for $\varepsilon_{\text{tol}} = 10^{-2}$. Although the circuit size has effectively doubled, the same $\delta_n \approx 10^{-3.5}$ is sufficient to get a converged estimate. Thus, every circuit must be probed independently! One cannot easily extrapolate convergence difficulty across different system sizes or trotter steps or even different rotation angles of the same circuit architecture.

Next, we turn to the more widely studied form of the dynamics Eq. (10) where the single qubit rotations are all correlated and equal to each other.

Here the details of the observable convergence are slightly different from the prior random angle case. However, many of the findings carry over. For example, we see that the largest fluctuations are already captured by the looser criteria of $\varepsilon_{\text{tol}} = 10^{-2}$. For the shallowest circuits, we converge very quickly regardless of the system size, but for the deepest circuits, there are small fluctuations which cause the convergence procedure to fail for $\varepsilon_{\text{tol}} = 10^{-3}$. We continue to observe the power law extrapolation of t versus δ . There is a significant transition in the runtime scaling around $\delta \sim 10^{-3}$.

As discussed previously, there is a strong dependence of convergence on ε , and we can see that the observable as a function of δ is non-monotonic. Thus, depending on the spacing r , you may encounter local minima, which falsely indicate convergence. For this set of circuits and this observable, around $\delta \approx 10^{-3}$ however, there appear to be fewer inflection points with large fluctuations. Additionally, due to the estimates being non-monotonic, there are no guarantees that convergence prevents larger fluctuations as δ continues to decrease.

⁷For large δ , a single core is faster due to communication overhead.

⁸Strictly speaking, the experiment for $T = 24$ did not converge when taking $\ell = 3$, pointing to the trial and error nature of defining convergence criteria.

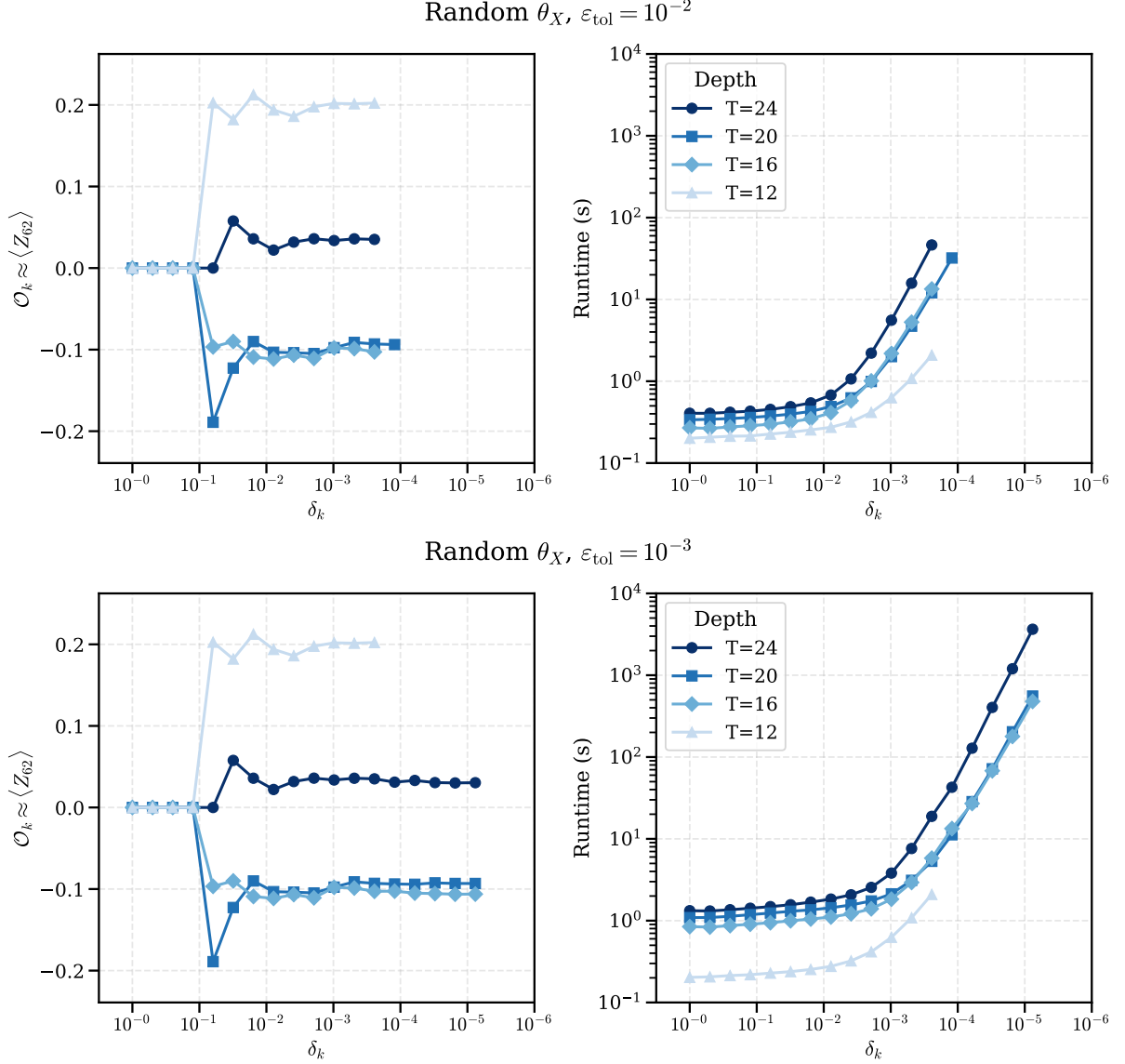


Figure 6: Convergence plots showing \mathcal{O}_k , the approximation to the expectation value $\langle Z_{62} \rangle$, as a function of δ_k with randomly sampled θ_X . The top row is with $\varepsilon_1 = 0.01$ and the bottom row is for a stricter $\varepsilon_2 = 0.001$. We vary the number of Trotter steps T within the range $[12, 24]$. The right column has the runtimes demonstrating a power law scaling with a transition in the exponent. Notably, $T = 16$ and $T = 20$ have nearly identical runtimes. With $T = 12$, the successive points converged at the same value of δ_k for both ε_1 and ε_2 . The offset in runtimes on the bottom row (for $T = 16, 20, 24$) are due to using a 64 CPU core vs a single CPU core due to smaller δ_k .

4.2 Beyond Apparent Convergence

PPS has been used to successfully reproduce expectation values consistent with quantum hardware experiments at modest δ [BC23]. However, applying our proposed convergence procedure yields an inconclusive result about the predicted value without priors from quantum hardware. The lack of convergence in these cases highlights the limitations on the utility of PPS as both a discovery and a verification tool.

PPS works best when there are fewer Pauli terms to track or when the truncated terms are significantly smaller than the surviving ones. Clifford circuits provide an extreme limit, mapping Pauli terms to single Paulis, so PPS is exact. The presence of magic [DKT24, RJT+25], or non-Cliffordness, thus is one proxy for the difficulty of PPS methods⁹. Indeed, when $\theta = \pi/4$, the branching in Eq. 9 yields equal weights.

In this section, we again study circuits from the quantum kicked Ising model. This time, we fix

⁹The name Sparse Pauli Dynamics (SPD) comes from this intuition

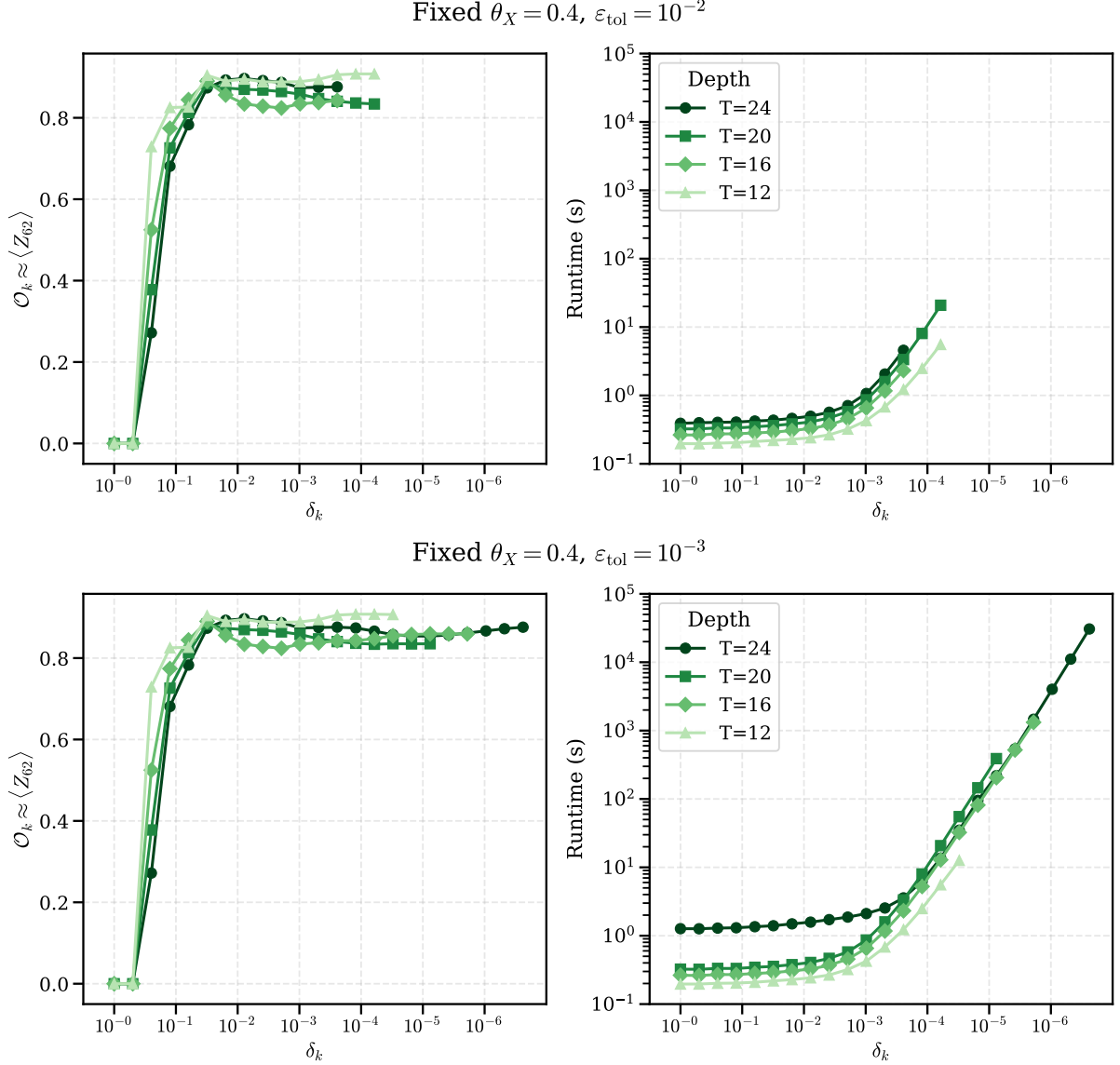


Figure 7: Convergence plots of \mathcal{O}_k with fixed $\theta_X = 0.4$. We vary the number of Trotter steps T within the range $[12, 24]$. For $\varepsilon_{\text{tol}} = 10^{-2}$ (top row), all experiments converge within 20s on a single CPU core. Changing to a stricter $\varepsilon_{\text{tol}} = 10^{-3}$, the estimated expectation value does not change significantly, but takes significantly longer to converge. The offset of $T = 24$ in the bottom row is again due to using a 64 core CPU.

$T = 20$ and instead vary the single qubit rotation angles θ_X between 0.3 and 0.7, slowly dialing up the magic or non-Cliffordness.

For $\theta_X = 0.3, 0.4$, we find that the observable converges with $\varepsilon_{\text{tol}} = 0.01$ within seconds as in the previous sections. However, as θ_X increases to 0.6, 0.7, we see that there are larger fluctuations even past $\delta = 10^{-3}$. This is the marked contrast from the previous convergence of observables, well into the regime that the power law scaling of runtime kicks in. The wide variance in values reported reflects the lack of reasonable error bounds for smaller delta. We also plot the publicly available data from the experiments in Ref. [K⁺23]. See Fig. 8.

The point we emphasize is that PPS here does not readily yield a prediction. One can estimate a range of values where the true expectation value is expected to live, but no single value stands out as more “accurate” a priori. Additionally, the lack of controlled error means that the final answer could live outside the range of previously computed estimates.

With a criteria of getting $\ell = 3$ successive points to agree within ε_{tol} , it’s clear at least two more data points are required. Extrapolating based on the power law scaling, we determine that the two additional

data points for $\theta_X = 0.6$ would require over 11 and 44 hours respectively and the two additional data points for $\theta_X = 0.7$ would require over 17 and 70 hours respectively. If the goal is to obtain a self-consistent answer rather than finding a δ which matches a known result, this would dramatically shift the narrative around the necessary classical resources. Rather than minutes on a laptop, it may require several days on a cluster.

IBM Reproduction

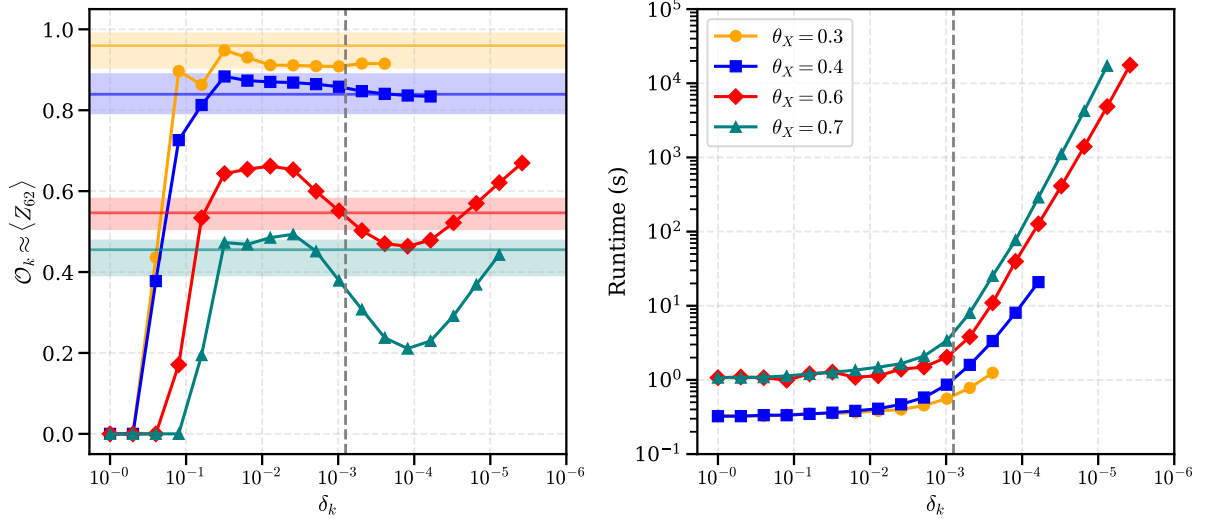


Figure 8: Convergence plots of O_k for $\theta_X = 0.3, 0.4, 0.6, 0.7$. We fix the number of Trotter steps $T = 20$ within the range. For $\varepsilon_{\text{tol}} = 10^{-2}$ (top row), the experiments corresponding to $\theta_X = 0.3, 0.4$ both converge within 20s on a single CPU core. However, the experiments corresponding to $\theta_X = 0.6, 0.7$ exhibit much larger fluctuations with decreasing δ_k and did not converge within the 10 hour limit we set on compute time for any single δ_k . We note that the latter pair of experiments were carried out on a 64 core CPU. The vertical dashed line indicates the truncation parameter used by Garnet as the single δ that approximates the quantum result across all angles.

The lack of convergence here also highlights the fact that a smaller δ does not translate in principal to a more accurate answer. Thus, it may be more beneficial to the user to perform a more coarse approximation with the understanding that the error bar might be somewhat significant.

5 Discussion

Pauli Path Simulation represents one of a handful of frontier classical methods for quantum simulation, offering unique capabilities for tackling utility-scale quantum circuits. Our work provides quantum researchers with a systematic framework for understanding when PPS delivers reliable estimates and where its fundamental limitations emerge.

Resource Prediction and Mathematical Structure One of our key contributions reveals the surprisingly elegant mathematical structure underlying PPS dynamics. A power-law distribution Eq. (11) can be used to approximately model the distribution of the absolute values of the Pauli coefficients corresponding to the evolved observable. This observation enables ballpark predictions of computational resource requirements using only brief and computationally inexpensive test runs. This discovery transforms resource estimation from guesswork into a principled extrapolation procedure, allowing researchers to predict memory and runtime scaling for finer truncation parameters δ without committing to expensive full simulations.

Counterintuitive Performance Characteristics Our convergence analysis reveals several surprising aspects of PPS behavior that challenge conventional intuition. Reducing the truncation parameter δ does not always improve accuracy, and deeper quantum circuits may actually converge more easily than shallower ones—effects we trace to the degree of non-Cliffordness in the evolution. These findings underscore the critical need for problem-specific benchmarking rather than attempting to extrapolate convergence difficulty across different system sizes, circuit depths, or parameter regimes. Each quantum simulation problem must be probed independently using our proposed convergence protocol.

Testing for Apparent Convergence Our systematic study reveals two distinct operational regimes for PPS. In the first regime, problems exhibit apparent convergence where successive refinements in δ lead to stable expectation value estimates with modest computational resources. In the second regime, PPS reports large fluctuations that do not readily yield a single answer. Surprisingly, some problems that successfully reproduce published IBM results actually fall into this second category when examined through our convergence lens, highlighting the distinction between post-hoc verification and independent prediction capability.

Practical Utility Beyond Apparent Convergence Even when PPS fails to achieve formal convergence, it retains significant practical value as a complementary tool to quantum hardware experiments. In the era of noisy intermediate-scale quantum devices, where error mitigation requires careful tuning of numerous parameters—noise models, gate selections for Pauli twirling, and mitigation protocols – PPS provides an independent classical estimate that can guide optimization efforts. For instance, if quantum results exhibit opposite signs from the entire PPS convergence trajectory, this signals potential issues with error mitigation parameters that warrant investigation.

The method proves particularly valuable in applications where approximate answers suffice. In the Sample-based Quantum Diagonalization method introduced in [RM⁺25], the precise energy estimate may matter less than capturing the correct amplitude weights for subspace population. Similarly, quantum machine learning applications often use expectation values as inputs to classical networks, where classification accuracy depends more on distinguishing between different examples than on precise numerical values. In these contexts, PPS serves as an inexpensive classical pre-training tool, with subsequent refinement possible on quantum hardware.

PPS also presents an economically attractive first solution. Since it is primarily CPU-based, experiments are significantly less expensive than GPU or QPU simulations. This can accelerate the research pipeline, providing insight into whether a problem is classically difficult and how much additional computational resources is needed to push to finer resolutions.

Implications for Quantum Advantage As quantum computing advances toward demonstrating practical quantum advantage, distinguishing between problems that succumb to improved classical methods and those requiring genuine quantum resources becomes increasingly critical. Our systematic framework for evaluating PPS—one of the most promising frontier classical simulation techniques—helps sharpen these boundaries. By providing reliable diagnostics for when classical simulation suffices versus when quantum hardware offers genuine advantages, this work contributes to the broader effort of mapping the quantum-classical computational landscape.

Rather than positioning this analysis as criticism of PPS, we view it as essential guidance for a powerful but nuanced simulation tool. The method’s relative novelty necessitates careful characterization of its capabilities and limitations. Our convergence protocol offers an inexpensive preliminary assessment that helps researchers determine whether their specific quantum simulation problem lies within the realm of classical tractability or genuinely requires quantum resources. This diagnostic capability becomes increasingly valuable as we approach the threshold of quantum computational advantage, providing a principled approach to distinguishing between classical and quantum regimes in contemporary quantum simulation challenges.

References

- [AGL⁺23] Dorit Aharonov, Xun Gao, Zeph Landau, Yunchao Liu, and Umesh Vazirani. A polynomial-time classical algorithm for noisy random circuit sampling. In *Proceedings of the 55th Annual ACM Symposium on Theory of Computing*, STOC ’23, page 945–957. ACM, June 2023.
- [AMR⁺25] Armando Angrisani, Antonio A. Mele, Manuel S. Rudolph, M. Cerezo, and Zoë Holmes. Simulating quantum circuits with arbitrary local noise using pauli propagation, 2025.
- [ASR⁺24] Armando Angrisani, Alexander Schmidhuber, Manuel S. Rudolph, M. Cerezo, Zoë Holmes, and Hsin-Yuan Huang. Classically estimating observables of noiseless quantum circuits. 9 2024.
- [BB17] Jacob Biamonte and Ville Bergholm. Tensor networks in a nutshell, 2017.
- [BC23] Tomislav Begušić and Garnet Kin-Lic Chan. Fast classical simulation of evidence for the utility of quantum computing before fault tolerance. 6 2023.

- [BevacC25] Tomislav Begušić and Garnet Kin-Lic Chan. Real-time operator evolution in two and three dimensions via sparse pauli dynamics. *PRX Quantum*, 6:020302, Apr 2025.
- [BGC23] Tomislav Begušić, Johnnie Gray, and Garnet Kin-Lic Chan. Fast and converged classical simulations of evidence for the utility of quantum computing before fault tolerance. *Sci. Adv.*, 10(3):adk4321, 2023.
- [DKT24] Neil Dowling, Pavel Kos, and Xhek Turkeshi. Magic of the Heisenberg Picture. 8 2024.
- [FRD⁺25] Enrico Fontana, Manuel S. Rudolph, Ross Duncan, Ivan Rungger, and Cristina Cîrstoiu. Classical simulations of noisy variational quantum circuits. *npj Quantum Inf.*, 11(1):84, 2025.
- [HCO⁺11] Jutho Haegeman, J. Ignacio Cirac, Tobias J. Osborne, Iztok Pizorn, Henri Verschelde, and Frank Verstraete. Time-Dependent Variational Principle for Quantum Lattices. *Phys. Rev. Lett.*, 107:070601, 2011.
- [HLO⁺16] Jutho Haegeman, Christian Lubich, Ivan Oseledets, Bart Vandereycken, and Frank Verstraete. Unifying time evolution and optimization with matrix product states. *Phys. Rev. B*, 94(16):165116, 2016.
- [K⁺23] Youngseok Kim et al. Evidence for the utility of quantum computing before fault tolerance. *Nature*, 618(7965):500–505, 2023.
- [LPR⁺24] Sacha Lerch, Ricard Puig, Manuel S. Rudolph, Armando Angrisani, Tyson Jones, M. Cerezo, Supanut Thanasilp, and Zoë Holmes. Efficient quantum-enhanced classical simulation for patches of quantum landscapes, 2024.
- [LWZ⁺23] Hai-Jun Liao, Kang Wang, Zong-Sheng Zhou, Pan Zhang, and Tao Xiang. Simulation of IBM’s kicked Ising experiment with Projected Entangled Pair Operator. 8 2023.
- [Orú14] Román Orús. A practical introduction to tensor networks: Matrix product states and projected entangled pair states. *Annals of Physics*, 349:117–158, 2014.
- [PJSO24] Siddhartha Patra, Saeed S. Jahromi, Sukhbinder Singh, and Roman Orus. Efficient tensor network simulation of IBM’s largest quantum processors. *Phys. Rev. Res.*, 6(1):013326, 2024.
- [QWE19] Hammam Qassim, Joel J. Wallman, and Joseph Emerson. Clifford recompilation for faster classical simulation of quantum circuits. *Quantum*, 3:170, August 2019.
- [RJT⁺25] Manuel S. Rudolph, Tyson Jones, Yanting Teng, Armando Angrisani, and Zoë Holmes. Pauli Propagation: A Computational Framework for Simulating Quantum Systems. 5 2025.
- [RM⁺25] Javier Robledo-Moreno et al. Chemistry beyond the scale of exact diagonalization on a quantum-centric supercomputer. *Sci. Adv.*, 11(25):adu9991, 2025.
- [SWCL24] Yuguo Shao, Fuchuan Wei, Song Cheng, and Zhengwei Liu. Simulating noisy variational quantum algorithms: A polynomial approach. *Phys. Rev. Lett.*, 133:120603, Sep 2024.
- [SYGY24] Thomas Schuster, Chao Yin, Xun Gao, and Norman Y. Yao. A polynomial-time classical algorithm for noisy quantum circuits. 7 2024.
- [TF23] Joseph Tindall and Matthew Fishman. Gauging tensor networks with belief propagation. *SciPost Physics*, 15(6), December 2023.
- [TFSS24] Joseph Tindall, Matthew Fishman, E. Miles Stoudenmire, and Dries Sels. Efficient Tensor Network Simulation of IBM’s Eagle Kicked Ising Experiment. *PRX Quantum*, 5(1):010308, 2024.
- [Vid03] Guifré Vidal. Efficient Classical Simulation of Slightly Entangled Quantum Computations. *Phys. Rev. Lett.*, 91(14):147902, 2003.

A PPS Convergence with BlueQubit Backend

This section contains the code snippet to use the BlueQubit backend for studying PPS convergence. After using qiskit to build the circuit of interest, one simply needs to specify the observable as well as successive δ_k . With relatively few runs, one can also perform the regression to extrapolate the time needed to go to finer δ . The code snippet shown below can be used to reproduce the PPS curve corresponding to $\theta_X = 0.3$ in Fig. 8

```
import bluequbit
import matplotlib.pyplot as plt
import numpy as np

# helper function that returns all the nearest neighbors on
# IBM's 127 qubit heavy hex lattice
from bluequbit.library.helpers.hardware_connectivites import
    IBM_127_HEAVY_HEX_MAP

# helper function that returns qiskit Pauli objects given the
# qubits idxs for the X,Y, and Z operators in the Pauli string
from bluequbit.library.helpers.pauli_sum import construct_pauli_from_idx_lists
from qiskit import QuantumCircuit

# you can get the BlueQubit API key after signing up at https://app.bluequbit.io
bq = bluequbit.init("<BLUEQUBIT API KEY>")

num_qubits = 127
num_trotter_steps = 20

rzz_angle = -np.pi / 2
rx_angle = 0.3

# list of the coefficient thresholds (delta) in decreasing order
deltas = [1 / 2**i for i in range(13)]

# list to store the expectation value <Z_62> for each choice of delta
expectation_values = []

# construct circuit for this pair of rzz and rx angles
qc = QuantumCircuit(num_qubits)
for _ in range(num_trotter_steps):
    for edge in IBM_127_HEAVY_HEX_MAP:
        qc.rzz(rzz_angle, edge[0], edge[1])
    for i in range(num_qubits):
        qc.rx(rx_angle, i)

for delta in deltas:
    # set the Pauli path coefficient threshold
    options = {
        "pauli_path_truncation_threshold": delta,
    }

    # run PPS
    expectation_values.append(
        bq.run(
            qc, device="pauli-path", pauli_sum=pauli_sum, options=options
        ).expectation_value
    )

plt.plot(-np.log10(deltas), expectation_values)
```

B Bit efficient representation of Pauli sums

We note that in the Pauli decomposition of the observable O_k , each Pauli $P \in \mathcal{P}_k$ admits the following symplectic representation:

$$P = (-i)^{\alpha_P} X^{x_P^{(1)}} Z^{z_P^{(1)}} \otimes X^{x_P^{(2)}} Z^{z_P^{(2)}} \otimes \dots \otimes X^{x_P^{(n)}} Z^{z_P^{(n)}}, \quad (22)$$

where $\alpha_P \in \mathbb{Z}$, X and Z denote the usual Pauli X and Z matrices respectively, and for each qubit ℓ we have the boolean pair $(x_P^{(\ell)}, z_P^{(\ell)}) \in \mathbb{Z}_2^2$. We define the boolean vector $\nu_P := (z_P^{(1)}, \dots, z_P^{(n)}, x_P^{(1)}, \dots, x_P^{(n)}) \in \mathbb{Z}_2^{2n}$. Thus, to efficiently represent the observable O_k in memory we can store two length $|P_k|$ arrays that contain the set of complex coefficients $\{c_P^{(k)}\}_{P \in \mathcal{P}_k}$ and integers that generate the phase factors $\{\alpha_P\}_{P \in \mathcal{P}_k}$, as well as a $|P_k| \times (2n)$ array such that each row contains a vector of the form ν_P ¹⁰.

As shown for instance in [BcvacC25], all the operations required to perform this evolution in the Heisenberg picture can be efficiently performed by manipulating the three arrays. For example, we can check the commutativity of two Pauli operators as follows. Let ν_P and $\nu_{\sigma_{k+1}}$ be the boolean vectors corresponding to the Pauli operators P, σ_{k+1} respectively. We define the quantity $s_{P\sigma_{k+1}}$ as follows:

$$s_{P\sigma_{k+1}} := \text{parity}(\nu_P[n:] \& \nu_{\sigma_{k+1}}[:n]) \oplus \text{parity}(\nu_P[:n] \& \nu_{\sigma_{k+1}}[n:]), \quad (23)$$

where $(\cdot) \& (\cdot)$ represents the bitwise AND operator, $(\cdot) \oplus (\cdot)$ represents the XOR operation (addition modulo 2), $\nu_P[n:]$ and $\nu_P[:n]$ represent the first and last (respectively) n components of the vector ν_P , and $\text{parity}(\cdot)$ returns the number of non-zero bits modulo 2. Upon computing $s_{P\sigma_{k+1}}$, the commutativity of P and σ_{k+1} can be determined as follows:

$$s_{P\sigma_{k+1}} = 0 \implies [P, \sigma_{k+1}] = 0 \quad (24)$$

$$s_{P\sigma_{k+1}} = 1 \implies \{P, \sigma_{k+1}\} = 0. \quad (25)$$

Hence, at every stage in the evolution, we can construct the sets $\mathcal{P}_k^{\text{comm}}, \mathcal{P}_k^{\text{anti}}$ by computing $s_{P\sigma_{k+1}} \forall P \in \mathcal{P}_k$. Products of the form $P' = \sigma_{k+1}P$ can also be efficiently constructed by using the symplectic representation in the following way:

$$\alpha_{P'} = \alpha_P + \alpha_{\sigma_{k+1}} + 2 \cdot \text{count}(\nu_P[:n] \& \nu_{\sigma_{k+1}}[n:]) \quad (26)$$

$$\nu_{P'} = \nu_P \oplus \nu_{\sigma_{k+1}}, \quad (27)$$

where $\text{count}(\cdot)$ returns the number of non-zero bits. Upon evolving the observable by all the unitaries in the set $\{U_j\}_{j \in [J]}$, the required expectation value is then given by

$$\langle O \rangle = \langle 0 | O_J | 0 \rangle = \sum_{P \in \mathcal{P}_J} c_P^{(J)} \langle 0 | P | 0 \rangle = \sum_{\substack{P \in \mathcal{P}_J \\ P=Z\text{-type}}} c_P^{(J)} (-i)^{\alpha_P}, \quad (28)$$

where the final sum only runs over the Z -type Paulis in P_J , i.e. Paulis for which the boolean vectors are of the form $\nu_P = (z_P^{(1)}, \dots, z_P^{(n)}, 0, \dots, 0)$.

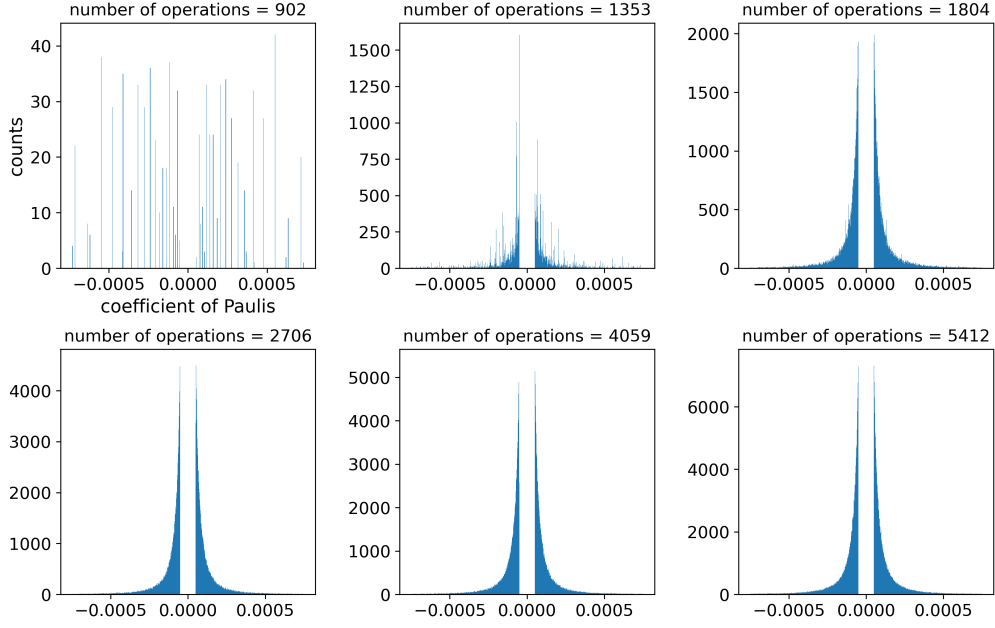
C Coefficient distribution for correlated angles

Fig. 2 shows that the distribution of the absolute values of the Pauli coefficients converges to a power law over the course of circuit evolution under the kicked Ising dynamics with θ_X chosen at random. Fig. 9 show that this feature is not restricted to completely random angles and can also be observed for fixed, correlated θ_X as well.

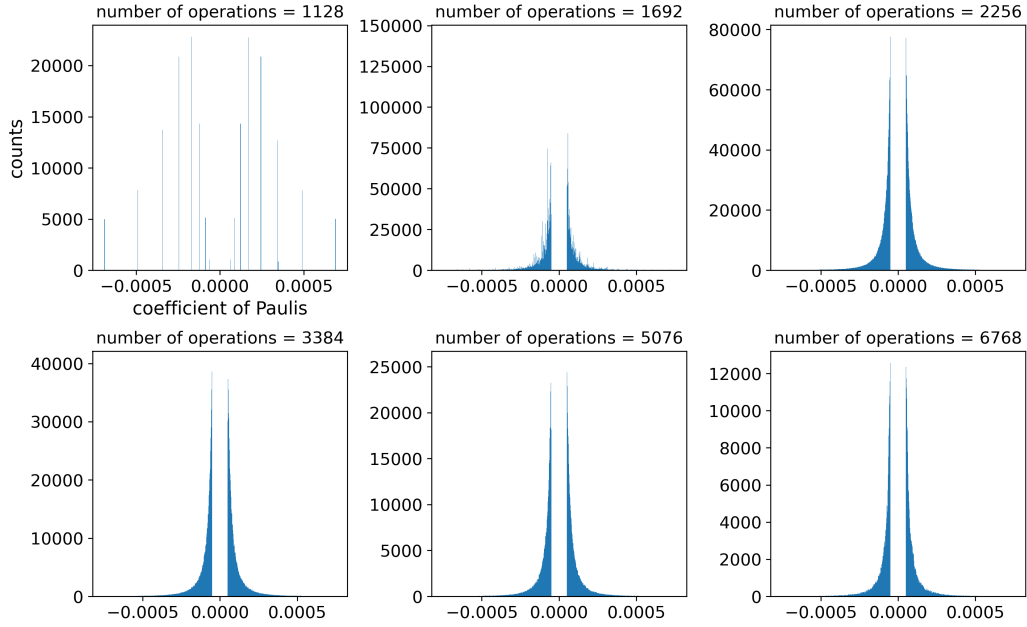
D Analytical results on Pauli Proliferation

For any Pauli operator P , with associated data (c_P, α_P, ν_P) , the scalar $(-i)^{\alpha_P - \text{sum}(\nu_P[:n] \& \nu_P[n:])} \times c_P$ is always real, and we shall abuse notation by denoting this quantity again by c_P (and refer to them as ‘real coefficients’ if necessary). These are the actual coefficients of the underlying Pauli string operators in

¹⁰In practice, we use the idea presented in [BGC23] to encode each vector ν_P into an array of 64 bit unsigned integers and hence the $2D$ array consisting of all such vectors can be stored as a $|P_k| \times (2\lceil n/64 \rceil)$ array



(a) Evolution for circuit with θ_X equal to $\pi/6$ and $T = 20$ for $\delta = 5 \times 10^{-5}$.



(b) Evolution for circuit with θ_X equal to $\pi/4$ and $T = 25$ for $\delta = 5 \times 10^{-5}$.

Figure 9: Evolution of the distribution of the Pauli coefficients of the evolved observable for circuits with correlated angles

the linear expansion of the observable in the Pauli basis. Consider the observable O_k defined in Eq. (5), generated by applying the first k unitary gates of the circuit shown in Eq. (3), followed by coefficient truncation at each step. We assume that the real coefficients $c_P^{(k)}$ are distributed according to a PDF $\rho_k : \mathbb{R} \rightarrow \mathbb{R}_{\geq 0}$:

$$\Pr(\alpha \leq c_P^{(k)} \leq \beta) = \int_{\alpha}^{\beta} \rho_k(x) dx. \quad (29)$$

By imposing a $\delta \in \mathbb{R}_{\geq 0}$ truncation threshold, we introduce the following constraint on ρ_k :

$$\rho_k(x) = 0 \quad \forall |x| < \delta. \quad (30)$$

We now ask the following question: How can we use ρ_k to determine the new PDF ρ_{k+1} used to describe the distribution of the numbers $c_P^{(k+1)}$ appearing in the Pauli decomposition of O_{k+1} obtained by applying the gate $U_{k+1} = e^{-i(\theta/2)\sigma}$ to O_k followed by truncation? For the purpose of answering this question, we may assume without loss of generality that the gate U_{k+1} is non-Clifford. We can compute an approximation to ρ_{k+1} by making the following simplifying assumptions:

Hypothesis. (PPS hypothesis)

- i.) The distribution satisfied by the numbers $c_P^{(k)}$ corresponding to Pauli operators in \mathcal{P}_k^{comm} and those corresponding to Pauli operators in \mathcal{P}_k^{anti} are the same, i.e. Eq. (29) holds with the same PDF ρ_k $\forall P \in \mathcal{P}_k^{comm}$ and $P \in \mathcal{P}_k^{anti}$.
- ii.) For the Pauli gate generator σ , define the set of Pauli operators $\sigma\mathcal{P}_k^{anti} \subseteq \mathcal{P}_{k+1}$ as follows:

$$\sigma\mathcal{P}_k^{anti} := \{\sigma P \mid P \in \mathcal{P}_k^{anti}\}. \quad (31)$$

The distribution of coefficients of Paulis in \mathcal{P}_k^{anti} induces by restriction a distribution on coefficients of Paulis belonging to $\mathcal{P}_k^{anti} \cap \sigma\mathcal{P}_k^{anti}$. Then, for any randomly chosen $P \in \mathcal{P}_k^{anti} \cap \sigma\mathcal{P}_k^{anti}$, we assume the following independence for the pair $\{P, \sigma P\} \subset \mathcal{P}_k^{anti} \cap \sigma\mathcal{P}_k^{anti}$:

$$\Pr(\alpha \leq c_P^{(k)} \leq \beta, \alpha' \leq c_{\sigma P}^{(k)} \leq \beta') = \Pr(\alpha \leq c_P^{(k)} \leq \beta) \times \Pr(\alpha' \leq c_{\sigma P}^{(k)} \leq \beta') \quad (32)$$

Remark. An important consequence of these assumptions is the following: Let $\mathcal{P}_{k+1} := \mathcal{P}_k^{comm} \cup (\mathcal{P}_k^{anti} \cup \sigma_{k+1}\mathcal{P}_k^{anti})$ be the new set of Pauli terms prior to truncation, and suppose $P' \in \mathcal{P}_{k+1}$ belongs to $\mathcal{P}_k^{anti} \cap \sigma\mathcal{P}_k^{anti}$. Let $P' = i\sigma P$ be such that Eq. (9) reads $c_{P'}^{(k+1)} = c_P^{(k)} \cos(\theta) + c_{\sigma P}^{(k)} \sin(\theta)$. Then

$$\Pr(\alpha \leq c_{P'}^{(k+1)} \leq \beta) = \Pr(\alpha \leq c_P^{(k)} \cos(\theta) + c_{\sigma P}^{(k)} \sin(\theta) \leq \beta) = \int_{\alpha}^{\beta} (\rho_k)_{\theta}^*(t) dt,$$

where

$$(\rho_k)_{\theta}^*(t) := |\sec(\theta)| \int_{-\infty}^{\infty} \rho_k(u) \rho_k(t \sec(\theta) - u \tan(\theta)) du \quad (33)$$

is the convolution.

Let us now estimate the number of Paulis remaining in \mathcal{P}_{k+1} after δ -truncation is applied to \mathcal{P}_{k+1} . Let $\varphi = |\mathcal{P}_k^{anti}|/|\mathcal{P}_k|$ be the fraction of Paulis in \mathcal{P}_k that anticommute with σ . And let $\eta = |\mathcal{P}_k^{anti} \cap \sigma\mathcal{P}_k^{anti}|/|\mathcal{P}_k|$ be the fraction of the anticommuting Paulis in \mathcal{P}_{k+1} that already exists in \mathcal{P}_k . From Eq. (9) the number of Paulis in $\mathcal{P}_k^{anti} \setminus \sigma\mathcal{P}_k^{anti}$, after truncation, gets reduced by a factor of $2 \int_{\delta \sec \theta}^{\infty} \rho_k(t) dt$. Likewise, $\sigma\mathcal{P}_k^{anti} \setminus \mathcal{P}_k^{anti}$ gets reduced by a factor of $2 \int_{\delta \csc \theta}^{\infty} \rho_k(t) dt$ and $\mathcal{P}_k^{anti} \cap \sigma\mathcal{P}_k^{anti}$ gets reduced by the factor $2 \int_{\delta}^{\infty} (\rho_k)_{\theta}^*(t) dt$.

Therefore, after the gate application and truncation, the number of Paulis $N_k := |\mathcal{P}_k|$ changes as

$$N_k \mapsto N_k (1 - \varphi + 2(\varphi - \eta) [\int_{\delta \sec \theta}^{\infty} \rho_k(t) dt + \int_{\delta \csc \theta}^{\infty} \rho_k(t) dt] + 2\eta \int_{\delta}^{\infty} (\rho_k)_{\theta}^*(t) dt) =: N'_k. \quad (34)$$

Note that N'_k is an approximation to N_{k+1} . Let us write $p(\theta) = 2 \int_{\delta \sec \theta}^{\infty} \rho_k(t) dt$, $q(\theta) = 2 \int_{\delta \csc \theta}^{\infty} \rho_k(t) dt$, and $r(\theta) = 2 \int_{\delta}^{\infty} (\rho_k)_{\theta}^*(t) dt$. Given the PPS hypothesis and the associated remark, for any $P \in \mathcal{P}_{k+1}$ we have

$$\begin{aligned}
\Pr(\alpha \leq c_P^{(k+1)} \leq \beta) &= [(\Pr(P \in \mathcal{P}_k^{comm}) + \Pr(P \in \mathcal{P}_k^{anti} \setminus \sigma \mathcal{P}_k^{anti}) + \Pr(P \in \sigma \mathcal{P}_k^{anti} \setminus \mathcal{P}_k^{anti}) \\
&\quad + \Pr(P \in \mathcal{P}_k^{anti} \cap \sigma \mathcal{P}_k^{anti})) \times \Pr(\alpha \leq c_P^{(k+1)} \leq \beta). \\
&= \frac{(1-\varphi)N_k}{N'_k} \Pr(\alpha \leq c_P^{(k)} \leq \beta) + \frac{(\varphi-\eta)N_k p(\theta)}{N'_k} \Pr(\alpha \leq c_P^{(k)} \cos(\theta) \leq \beta) \\
&\quad + \frac{(\varphi-\eta)N_k q(\theta)}{N'_k} \Pr(\alpha \leq c_P^{(k)} \sin(\theta) \leq \beta) + \frac{\eta N_k}{N'_k} \Pr(\alpha \leq c_P^{(k)} \cos(\theta) + c_{P'}^{(k)} \sin(\theta) \leq \beta).
\end{aligned} \tag{35}$$

$$\tag{36}$$

Thus, we see that the probability distribution function ρ_{k+1} of coefficient of Paulis in \mathcal{P}_{k+1} (after truncation) is related to that of \mathcal{P}_k by

$$\rho_{k+1}(t) = \frac{((1-\varphi)\rho_k(t) + (\varphi-\eta)[p(\theta)\sec(\theta)\rho_k(\sec(\theta)t) + q(\theta)\csc(\theta)\rho_k(\csc(\theta)t)] + \eta(\overline{\rho_k})_\theta(t))}{(1-\varphi + (\varphi-\eta)(p(\theta) + q(\theta)) + \eta r(\theta))}, \tag{37}$$

where $(\overline{\rho_k})_\theta(t)$ is the δ -truncation of the convolution $(\rho_k)_\theta^*(t)$ defined as $(\overline{\rho_k})_\theta(t) = (\rho_k)_\theta^*(t)$ if $|t| \geq \delta$, and $(\overline{\rho_k})_\theta(t) = 0$ otherwise.

Having derived the general equation governing the transformation of ρ_k , we now switch to the specific case of the power-law distribution Eq. (11). For the power-law distribution, we have $p(\theta) = (\cos \theta)^m$ and $q(\theta) = (\sin \theta)^m$. While $r(\theta)$ does not seem to have a simple form, it can be computed effectively with numerical integration as shown in Fig. 10. Eq. (34) can now written as:

$$N'_k = N_k(1 - \varphi + (\varphi - \eta)((\cos \theta)^m + (\sin \theta)^m) + \eta r(\theta)). \tag{38}$$

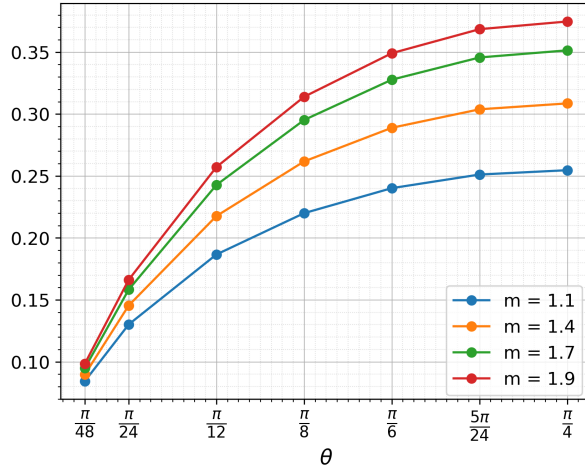


Figure 10: Plots showing the numerical value of $s(\theta) := \int_{-\delta}^{\delta} \rho_\theta^*(t) dt$ for the convolution Eq. (33) for different values of m . Under the PPS hypotheses, the set $\mathcal{P}^{anti} \cap \sigma \mathcal{P}^{anti}$ gets shrunk by the factor $1 - s(\theta)$ after applying a δ -truncation. This factor is denoted by $r(\theta)$ in the text, and it intervenes in Eq. (38). Due to the symmetry satisfied by ρ_θ^* , $s(\theta)$ satisfies $s(\pi/4 - \theta) = s(\pi/4 + \theta)$.

To maintain concise notation in this appendix, the dependence of φ, η , and m on k is implied and not explicitly noted. We point out that the above recurrence model, which we derived using properties of the power-law distribution, captures the similarity of the Pauli-growth curves seen in Figs. 5 and 11 (for large enough values of k , when the distribution is well-formed). The dependence of the model on δ arises implicitly through m, φ , and η . If there was no such dependence, Eq. (38) implies that the curves must be identical (translates). Numerical evidence, as shown in Fig. 3 and the insets of Fig. 12, suggests that the variation of m, φ , and η with respect to δ , though very subtle, is small and gradual. While these observations neatly explain why adjacent curves are so similar, they also suggest that Eq. (38) may be impractical for estimating the full Pauli growth curve.

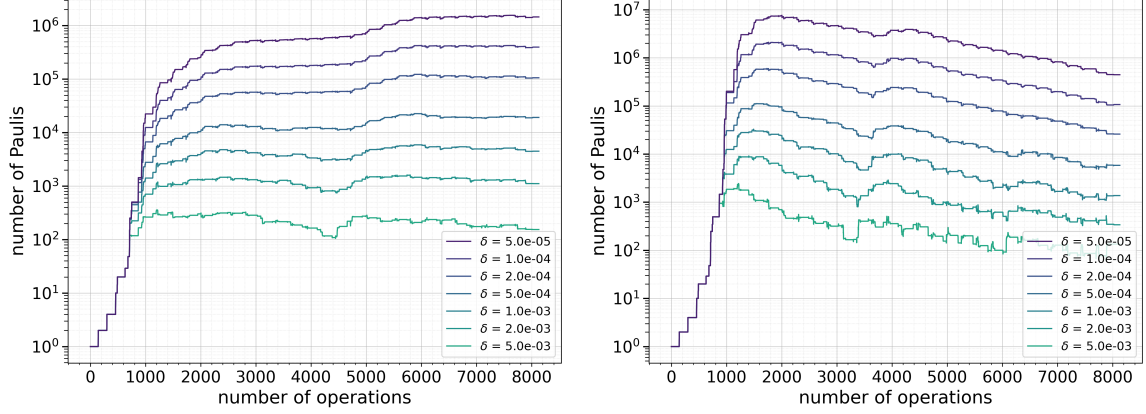


Figure 11: Growth of Paulis over the execution of the circuit. Left: for circuit with θ_X equal to $\pi/6$. Right: for θ_X equal to $\pi/4$. We set $T = 30$ for both. A standout feature of these plots is the regularity of the growth curves with respect to δ ; the curves are almost identical for smaller values of δ . This aspect of the simulation is explained by our modeling (see Eq. (38) and the subsequent discussion).

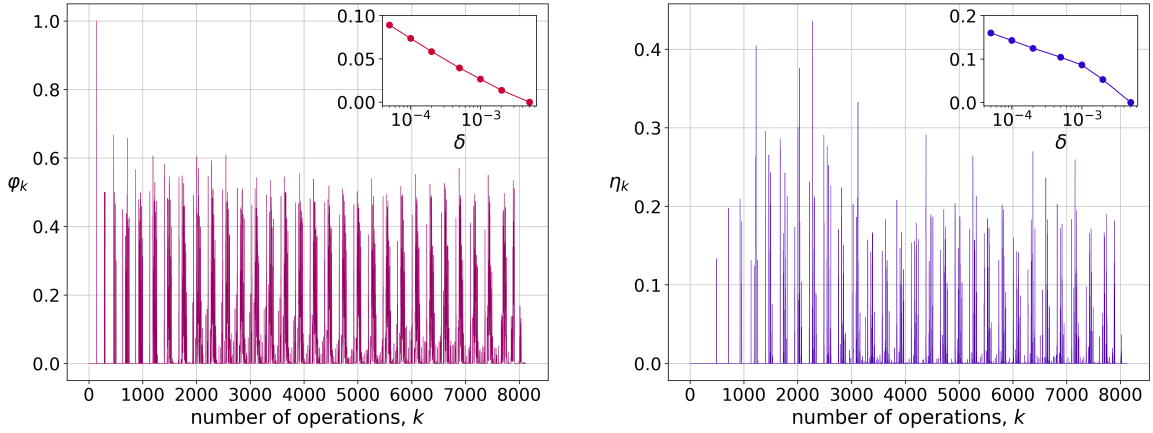


Figure 12: Fraction of anticommuting Paulis, $\varphi_k = |\mathcal{P}_k^{anti}|/|\mathcal{P}_k|$, and “existing” anticommuting Paulis, $\eta_k = |\mathcal{P}_k^{anti} \cap \sigma \mathcal{P}_k^{anti}|/|\mathcal{P}_k|$, plotted over the course of the circuit execution for the circuit constructed with each θ_X sampled uniformly from $[-\pi/4, \pi/4]$, $T = 30$ steps. The simulation is performed using $\delta = 5 \times 10^{-5}$. We see that η spikes a few times in each Trotter step. There is an η -spike at $k = 2036$, and we show its effect on the distribution in Fig. 14. Inset, left: Cosine distance (defined as $1 - \text{cosine similarity}$) between $\vec{\varphi}(\delta)$ and $\vec{\varphi}(\delta_0)$ as δ varies from $\delta_0 = 5 \times 10^{-3}$ to 5×10^{-5} . Here, we have interpreted the sequence $(\varphi_k)_{k=1,2,\dots,J}$ as a vector $\vec{\varphi}$. Inset, right: Variation of Cosine distance between $\vec{\eta}(\delta)$ and $\vec{\eta}(\delta_0)$. We observed in our experiments that the variation of $\vec{\varphi}$ and $\vec{\eta}$ with respect to δ is small and gradual.

Let us now turn to the distribution itself. For the power-law model, Eq. (37) which gives the changed density function reads

$$\rho_{k+1}(t) = \frac{([1 - \varphi + (\varphi - \eta)((\cos \theta)^{2m} + (\sin \theta)^{2m})]\rho_k(t) + \eta(\overline{\rho_k})_\theta(t))}{(1 - \varphi + (\varphi - \eta)((\cos \theta)^m + (\sin \theta)^m)) + \eta r(\theta)}. \quad (39)$$

Suppose for now that $\eta \ll 1$. Then, after ignoring the term $\eta(\overline{\rho_k})_\theta(t)$ above, the changed density function is of the form

$$\rho_{k+1}(t) \approx \lambda \rho_k(t) \quad (40)$$

for some constant λ depending on φ, η, θ and m . Thus, under the PPS hypothesis and the assumption that $\eta \ll 1$, we see that the functional form of the density function (power law) remains invariant under the dynamics. In fact, imposing the normalization condition on ρ_{k+1} implies that $\rho_{k+1} \approx \rho_k$. This is in fact consistent with numerical evidence.

The effect of the convolution term $\eta(\overline{\rho_k})_\theta(t)$ on the dynamics is more subtle. Although we can ignore this term when $\eta \ll 1$ or when $\theta \approx 0$ (in which case $(\overline{\rho_k})_\theta(t) \approx \rho_k(t)$) when considering a single step of the evolution, the cumulative effects over many gate applications can be significant. Furthermore, there could be many instances/gates when η spikes to high values (resulting in large merges in the step $\mathcal{P}_k \rightarrow \mathcal{P}_{k+1}$).

E Deviations from a Power Law caused by η -spikes

In this section, we discuss two possible effects related to the η dependent term in Eq. (38) that we have observed that lead to large visually apparent deviations of the distribution of the absolute values of the Pauli coefficients of the evolved observable from a power law. In particular these effects cause either transient or persistent deviations.

E.1 Transient deviations

For ease of notation, we shall denote the truncated convolution $(\overline{\rho_k})_\theta$ simply by $\bar{\rho}_\theta$. A priori, the effect of the term $\eta\bar{\rho}_\theta$ in Eq. (39) is not obvious; it is also unclear how this term propagates and skews the coefficient distribution evolution throughout circuit execution. We do know, however, from numerical evidence (for the IBM circuits with Clifford RZZ gates that we have considered here) that the truncated power-law distribution is persistent and any perturbation to it seems transient. This begs the question: how to explain away the effect of $\eta\bar{\rho}_\theta(t)$ in Eq. (39) and retain the stability of the truncated power-law distribution for the dynamics in circuits considered thus far?

It is important to tackle this problem for a fuller understanding of the dynamics of the distribution, as the approximation $\eta \ll 1$ is not always available. See Fig. 12 for an example. To better understand the convolution ρ_θ^* , we first observe that it has the same asymptotic tail as $\rho(t)$. In fact, for any t satisfying $|t| > 4\delta$, the approximation $\rho_\theta^*(t) \approx \rho(t)$ is a good one, with the error in approximation getting smaller as we move along the tail of the distribution. We refer to Fig. 13 to understand the qualitative nature of these convolutions as θ varies.

The plots in Fig. 13 and the sparseness of η -spikes in Fig. 12 suggest the following explanation as to why the power-law distribution is stable under perturbation under some mild conditions: The truncation $\bar{\rho}_\theta$ of ρ_θ^* , which modifies ρ as specified by Eq. (39), shares the same tail of ρ , but diverges from ρ in the region $\delta \leq |t| \leq 2\delta$, where it has a wiggle. This wiggle gets scaled by η and is added to ρ_{k+1} ; see Fig. 14. However, since these perturbations occur close to the edge of the δ -chasm, the wiggle quickly disappears (by branching followed by truncation) after the application of the next few gates. (Actually, a part of the wiggle lives on in the commutative part of the distribution. But after each subsequent gate application, this part gets diminished exponentially due to scrambling—as commuting Pauli terms for different gates are likely to be independent.)

In the above argument, we have implicitly assumed that there is a gap to the next η -spike, and furthermore that the rotation angles of the gates that immediately follow are not too small (modulo $\pi/2$). We next discuss what may happen if these assumptions fail.

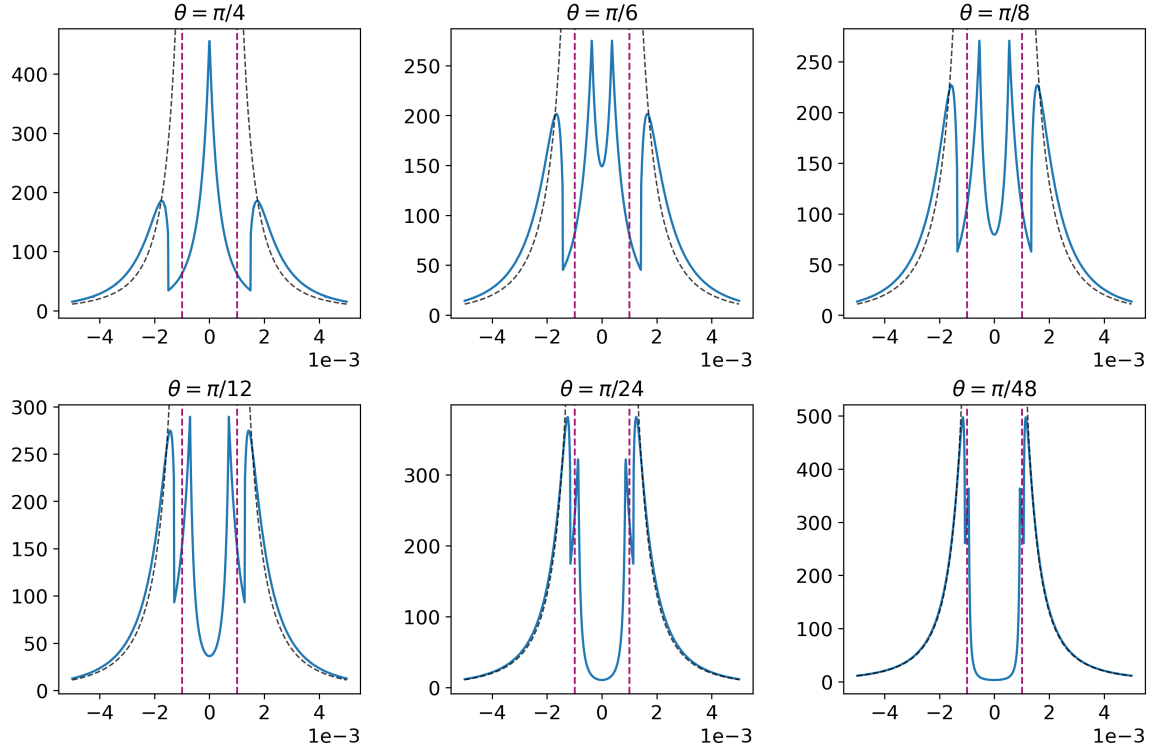


Figure 13: The convolution ρ_θ^* , defined in Eq. (33), for various values of θ . The plots are generated for ρ corresponding to the choice of $m = 1.7$, and $\delta = 10^{-3}$. While m affects the steepness of the curves, δ has no effect on the nature of these curves. The vertical lines correspond to $\pm\delta$. Also shown (in gray) is the original distribution $\rho(t)$. Under the PPS hypothesis introduced in App. D, coefficient distribution of Pauli terms belonging to $\mathcal{P}_k^{anti} \cap \sigma\mathcal{P}_k^{anti}$ is given by the truncation $\overline{(\rho_\theta^*)}$ of ρ_θ^* , defined as $\overline{(\rho_\theta^*)}(t) = \rho_\theta^*(t)$ if $|t| \geq \delta$, 0 otherwise. As seen above, the effect of convolution is manifested as a reduction of density (depending on θ) in the region between δ and 2δ . We note that as $\theta \rightarrow 0$, $\rho_\theta^* \rightarrow \rho$. Also, ρ_θ^* is symmetric about $\theta = \pi/4$: $\rho_{\pi/4-\theta}^* = \rho_{\pi/4+\theta}^*$ and hence we have omitted plots for θ in the range $(\frac{\pi}{4}, \frac{\pi}{2})$.

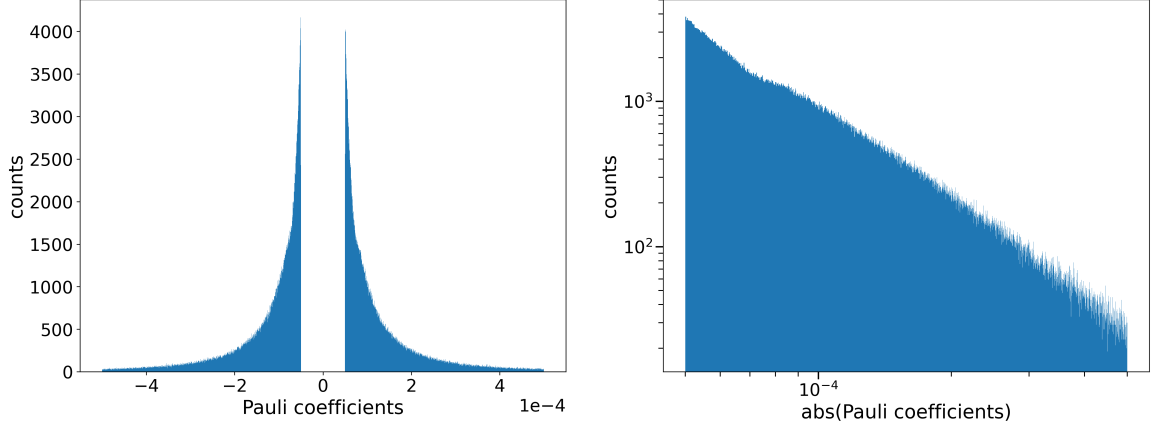


Figure 14: η -wiggle: These plots show the presence of a transient wiggle caused by an η -spike in the Pauli coefficient distribution ρ . The circuit we use is constructed with each θ_X sampled uniformly from $[-\pi/4, \pi/4]$ and $T = 30$. The simulation is performed using $\delta = 5 \times 10^{-5}$. We notice a wiggle in the distribution of the absolute values of the Pauli coefficients between δ and 2δ , as explained in Appendix E.1. This snapshot of coefficients is taken after the application of 2036 of the 8130 gates. At the 2036th gate, there is an η -spike with $\eta \approx 0.368$ caused by a rotation gate with angle approximately 55.13° . However, this wiggle disappears quickly within the next few gate applications.

E.2 Small angles and persistent deviations

In this section we discuss scenarios where at some point in the circuit execution η -spikes occur in a consecutive and persistent manner. In such a situation, the distribution ρ will be dominated by ρ_θ^* and its higher convolutions $((\rho_\theta^*)_\theta^*, \text{etc.})$, and this could alter the distribution ρ in such a way that it does not recover its power-law shape.

Even if the η -spikes are not consecutive, there can be cumulative effects seen over the course of many gate applications. The speed with which the wiggles produced by η -spikes get diminished (and eventually disappear) depends on the sequence of rotation angles of the subsequent gates. Since existing coefficients either remain the same (commutative case) or get multiplied by $\cos(\theta_j)$, smaller angles mean that the wiggles persist longer, thereby distorting the distribution via the compounding of self-convolutions.

We have in fact observed such instances of large deviation from the power law for modifications of the kicked Ising model IBM circuit where in all rotation angles, including the RZZ-angles, are small and correlated. See Fig. 15. Even in such cases, we notice that the tail of the distribution follows a power law (with $x_{\min} = l\delta$, for some l independent of gate k). The estimates and analysis from Section 3.2 carry over with only minor modifications to such cases.

F Challenges in estimating the power-law exponent m

We point out some challenges in estimating the power-law exponent m for the coefficient distribution. First, we notice that when using linear regression on log-log plots, starting at δ leads to an underestimation of m , due to a subtle reduction in density in the interval between δ and 2δ . We observe this deviation even when the coefficient distribution visually resembles a power-law shape as in Fig. 16. We suspect the cumulative effects caused by η -spikes as the reason behind this phenomenon, as we explained in E.2 where we provided visually apparent examples of this effect.

A more accurate approach to estimating m is to use the maximum likelihood estimate (MLE), given by

$$\hat{m}_k = \frac{N_k}{\sum_P \log(|c_P^{(k)}|/\delta)}. \quad (41)$$

This also leads to a similar underestimation of m . See Fig. 17. Since a key motivation for estimating the distribution parameter is to have accurate estimates for N_{\max} via Eq. (17), perhaps another way to estimate m would be a modification of the linear regression method, with the ‘continuous part’ of the tail weighted more—with weights proportional to the contribution to the observable norm-squared, as in Fig. 16. (We did not attempt to implement this method.)

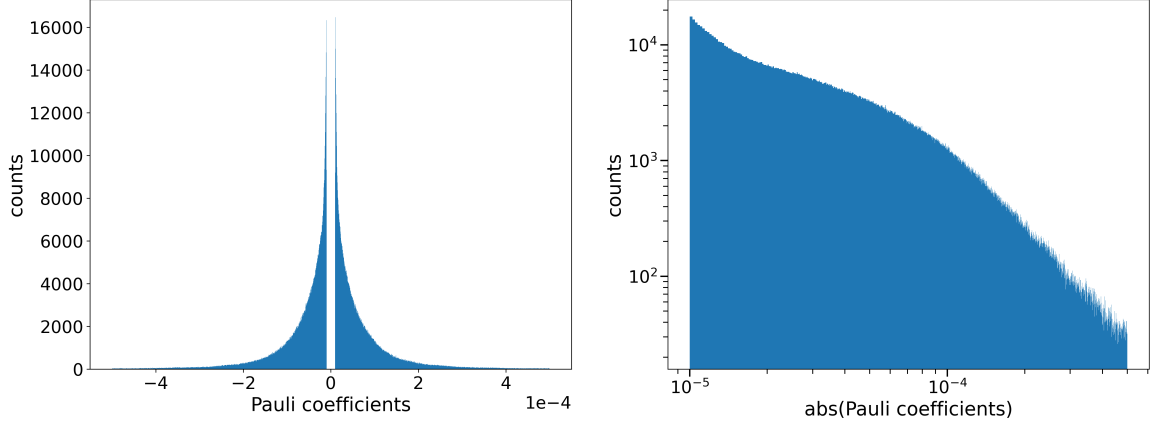


Figure 15: Plots corresponding to an experimental set up that exhibits visual deviations from a power-law distribution. Unlike in the rest of this work we choose the two qubit rotation angles to be non-Clifford. We set $\theta_{ZZ} = -\pi/36$, $\theta_X = \pi/12$, $T = 30$, and perform the simulation using $\delta = 10^{-5}$. The distributions shown are captured upon simulating all the gates in the circuit. Since the two-qubit rotations are chosen to be non-Clifford, they too contribute to η -spikes thus increasing their frequency. Because of the small angles involved, the effect of the convolution term in Eq. (39) persist longer, and this eventually leads to a distribution as shown above. The tail of the distribution, which contributes a majority to observable norm-squared, is still linear. We note here that the coefficient distribution for the 11×11 2D Ising model circuit from [BcvacC25] that we considered in Section 3.3 closely resembles the distribution above. Thus such a distorted distribution seems to arise intrinsically from the dynamics of Eq. (9) and furthermore appears to be stable.

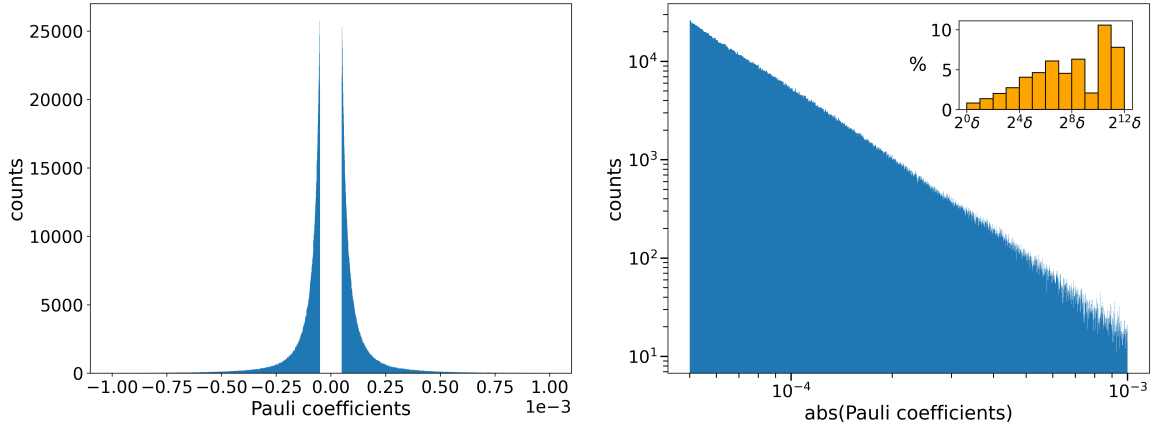


Figure 16: Distribution of Pauli coefficients for fixed θ_X equal to $\pi/6$, $T = 35$, and $\delta = 5 \times 10^{-5}$. The coefficients are captured at the end of the simulation. Inset (right): percentage contribution to norm-squared of the evolved observable, $\|O_k\|^2$ from coefficients c_P belonging to intervals $2^j \delta \leq |c_P| < 2^{j+1} \delta$, for $j = 0, 1, 2, \dots$. We note that there is a single coefficient that lies beyond $2^{13} \delta$ that contributes to around 47% of the norm, which is not shown. We see that the tail of the distribution dominates $\|O_k\|^2$.

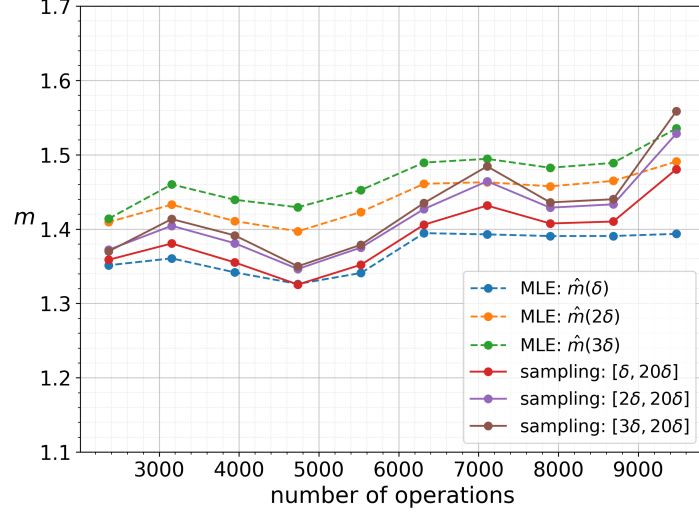


Figure 17: Plots showing variation of the power-law exponent m within the circuit for the same circuit set up as in Fig. 16, and for different estimation techniques. For the sampling method, similar to Fig. 3, we use bins of size $\delta/16$ centered at 144 uniformly spaced points x between $l\delta$ and 20δ , for each $l = 1, 2$, and 3, and use linear regression to find $m+1$ as the slope of $\log(\text{density})$ vs $\log(x)$. Alternatively, one can use maximum likelihood estimators for m , $\hat{m}(l\delta)$, given by variants of Eq. (41), with $x_{\min} = l\delta$ instead of δ . This amounts to ignoring all terms less than $l\delta$ (but keeping all of the tail).

Taking into account the aforementioned decrease in density in the leftmost part of the (absolute) distribution, we can parametrically estimate m , starting from $l\delta$, where $l = 1, 2, 3, \dots$ (l can also be any real multiple of δ). Likewise, one can consider maximum likelihood estimators $\hat{m}_k(l\delta)$, with x_{\min} set to $l\delta$; i.e., we replace δ with $l\delta$ in Eq. (41) and consider only those P that satisfy $|c_P^{(k)}| \geq l\delta$. These estimates are shown in Fig. 17. We did not explore the question of finding the optimal l (or x_{\min}) for the underlying distribution of Pauli coefficients $\{c_P^{(k)} \mid P \in \mathcal{P}_k\}$.

We conclude by noting that the discrepancy between various estimates in Fig. 17 points to statistical difficulties in estimating m as well as to subtle deviations from the hypothesized power-law distribution.